Received: 10 April 2018 | Revised: 17 December 2018 | Accepted: 20 December 2018

DOI: 10.1002/qj.3466

RESEARCH ARTICLE

Quarterly Journal of the Royal Meteorological Society RMetS

An adaptive background error inflation method for assimilating all-sky radiances

Masashi Minamide | Fuqing Zhang

Department of Meteorology and Atmospheric Science & Center for Advanced Data Assimilation and Predictability Techniques, The Pennsylvania State University, University Park, Pennsylvania

Correspondence
Fuqing Zhang, Department of Meteorology and Atmospheric Science, The Pennsylvania State University, University Park, PA 16802, USA.
Email: fzhang@psu.edu

Funding information
Japan Funai Foundation for Information Technology, n/a. National Aeronautics and Space Administration, NNX16AD84G and NNX15AQ51G. Office of Naval Research, N000141512298 and N000141812517. NASA, NNX15AQ51G, NNX16AD84G.

An adaptive background error inflation (ABEI) method is proposed for assimilating all-sky satellite brightness temperatures with an ensemble Kalman filter. This empirical cloud-scene-dependent covariance inflation method is designed to mitigate the model's difficulties in initiating convection in the observed cloudy regions where the background prior estimated from the ensemble mean incorrectly simulates clear-sky conditions. This new approach calculates a spatially varying, flow-dependent, multiplicative ensemble covariance inflation factor based on error statistics produced by a well-constructed, off-line observing system simulation experiment (OSSE) that assimilates similar all-sky radiance observations but were generated by the model, in which case the truth is known for all the state variables and the assimilated radiances. The adaptive inflation factor is a linear function of a cloud parameter which is only applied to the observed cloudy regions where there are less or no cloud in the prior ensemble mean estimates. The performance of ABEI is evaluated through assimilating synthetic and real-data all-sky radiance experiments from the Advanced Baseline Imager on board GOES-16 for Hurricanes *Karl of 2010* and *Harvey of 2017*. Assimilation experiments with ABEI allow adaptive inflation of the ensemble covariance in the model-simulated clear-sky regions when there are observed clouds while avoiding unnecessarily large ensemble spread in other cloud scenarios. This new approach alleviates the difficulty in estimating the appropriate inflation factors in the model state space using the innovation statistics in the observation space (radiance) with a highly nonlinear observation operator. It serves as an alternative to existing methods using spatially varying adaptive inflations; their relative performance and potential combinations are to be further assessed in the future.

KEYWORDS
all-sky satellite radiances, covariance inflation, ensemble Kalman filter

1 | INTRODUCTION

The ensemble Kalman filter (EnKF) has been used for data assimilation in high-dimensional, multi-variable geophysical applications. The EnKF estimates the flow-dependent background error covariance through a short-term ensemble, whose accuracy may be subject to various sources of uncertainties such as from using an insufficient ensemble size, inadequate representation of model errors, and the linear assumptions of the forecast model and forward observation operators which are usually nonlinear. If the ensemble spread underestimates the prior uncertainty, the filter may give too high a weight to the prior state, which can degrade the filter performance and potentially lead to filter divergence.

Covariance inflation is often designed to mitigate the inconsistent relationship between ensemble spread and the deviation of their mean from the true state. The multiplicative type of covariance inflation linearly increases the distance of the ensemble state from its mean by multiplying by a specific factor (Anderson, 2007; 2009; Li *et al.,* 2009; Gharamti, 2018). The additive covariance inflation adds climatological background perturbations into the ensemble prior estimates. Some studies indicated that multiplicative inflations are more suitable to deal with the assimilation errors related to the

observation networks, while the additive inflations can better mitigate model errors (e.g. Mitchell and Houtekamer, 2000).

Alternatively, there are methods to increase the posterior ensemble spread by relaxing the posterior perturbations to prior perturbations (i.e. relaxation-to-prior-perturbations, or RTPP: Zhang *et al.,* 2004; Ying and Zhang, 2015), or to prior spread (i.e. relaxation-to-prior-spread method, or RTPS: Whitaker and Hamill, 2012). Because the EnKF posteriors are updated with statistical correlations without explicit dynamical constraints, RTPP is reported to be able to restore the dynamical balance by mixing posterior perturbations with prior perturbations, which are constrained by the dynamics of the forecast models (Zhang *et al.,* 2004; Ying and Zhang, 2015).

Although inflations can be effective in maintaining the ensemble spread, tuning various parameters in the filter configurations through trial-and-error can be very costly. To avoid this costly process, various adaptive methods to estimate the parameters within each data assimilation cycle have been explored, often using the innovation (observation-minus-background, or O−B) statistics calculated in the observation space (Dee, 1995; Desroziers *et al.,* 2005; Li *et al.,* 2009). These adaptive inflation methods were further extended from estimating temporally varying optimal inflation factors to those including spatial variations. Anderson (2009) proposed an adaptive covariance inflation (ACI) method that uses a Bayesian approach to estimate temporally and spatially varying multiplicative covariance inflation factors. Similarly, spatially varying adaptive relaxation methods have also been explored through utilizing the ensemble spread reductions as a spatial mask for inflation (Whitaker and Hamill, 2012; Ying and Zhang, 2015; Kotsuki *et al.,* 2017). The underlying premise of these spatially varying covariance inflations is to estimate an optimal inflation factor in densely observed regions, which are often associated with a large ensemble spread reduction, while managing to keep the less-observed regions uninflated. To a varying degree of effectiveness, these aforementioned spatially varying inflation methods such as ACI, RTPP and RTPS may mask out the unobserved regions under the unevenly distributed observation networks, while inflating the regions with too large a spread reduction.

All-sky satellite observations can potentially bridge the physical gaps of those irregular observation networks, since, in particular, geostationary satellites have a contiguous spatial and temporal coverage. There is ongoing research reporting the promising potentials of assimilating all-sky satellite radiances in improving numerical weather predictions (Bauer *et al.,* 2006; 2011; Otkin, 2010; 2012; Auligné *et al.,* 2011; Zhang *et al.,* 2016; Honda *et al.,* 2018; Minamide and Zhang, 2018). For example, Jones *et al.* (2013; 2014) and Otkin (2010; 2012) conducted observing system simulation experiments (OSSEs) with simulated Geostationary Operational Environmental Satellite Advanced Baseline Imager (GOES-R ABI) infrared radiances that found positive impacts of assimilating these radiances under both clear and cloudy sky scenes, especially for upper-level clouds. Zhang *et al.* (2016) applied the assimilation of all-sky infrared satellite radiances onto the tropical cyclones (TCs) inner-core initialization with a convection-permitting model for the first time; they demonstrated the potential impacts of all-sky radiance assimilation in capturing the TC inner-core structures over the tropical ocean with sparse observation networks.

By classifying radiances into clear-sky and cloudy-sky in a binary manner,[1] the cloud scenes in assimilating all-sky radiances can be classified into four categories. The first category contains scenes in which both the observation and model prior are classified as clear-sky, which includes studies that masked out the cloud-affected observations and model priors (e.g. Zou *et al.,* 2013; 2015; Wang *et al.,* 2015). The second category contains scenes in which both observation and model prior are cloudy. This scene involves the cloud-affected radiance but with small to modest innovations (observation minus background or O−B). The remaining two categories consist of cases in which there is a mismatch between the observation and the model prior estimate. Given strong nonlinearities in the radiative transfer models, a large O−B innovation due to the mismatch can occur far more frequently than predicted by assuming a Gaussianity distribution. Although the probability distribution of the O−B innovation statistics for the cloud-affected radiances is reported to often follow a Gaussian-like distribution within a range of two to three times the observation error, those large innovations may also result in fat-tailed probability distributions in the observation space (Geer and Bauer, 2011; Okamoto *et al.,* 2014; Harnisch and Weissmann, 2016; Minamide and Zhang, 2017; Honda *et al.,* 2018). Moreover, these probability distributions in the observation space are reported not to always correspond to the distributions in the model state space in the case of a highly nonlinear observation operator (Minamide and Zhang, 2017).

Although both of the mismatched scenes (i.e. where the background prior estimated from the ensemble mean (incorrectly) simulates clear-sky conditions or cloudy conditions) can have similarly large O−B innovations, studies have indicated that there are asymmetric features between these two scenes (Vukicevic *et al.,* 2004; Errico *et al.,* 2007; Bauer *et al.,* 2010). For example, Vukicevic *et al.* (2004) showed that assimilation of infrared brightness temperatures (BTs) from the 10.7 μm channel on GOES-9 can effectively eliminate spuriously modelled clouds, but has difficulty in developing clouds in spuriously modelled clear-sky regions. Errico *et al.* (2007) attributed such difficulties in developing cloud and precipitation properties in the clear sky to the "zero-gradient" problem, which means the Jacobian of the observation

[1] Strictly speaking, the binary classification does not accurately represent the physical conditions, because radiances (and associated brightness temperatures) are continuous variables gradually changing from high (∼ clear-sky) values to low (∼ high clouds) values. The method to deal with this continuity is discussed in section 3.1.

operator may become zero when the observable is zero. The different characteristics of these four types of scene contribute to developing heteroscedasticity (i.e. flow-dependent spatial variation) of the innovation statistics.

In this study, we explore how these innovation statistics change among different cloud scenes and propose a new inflation method to deal with the asymmetry among cloud scenes. We propose to empirically obtain an optimal multiplicative inflation factor using the output of observing system simulation experiments (OSSEs). The performance of this newly proposed inflation method with cloud-scene-dependent adaptive background error inflation (hereafter called ABEI) is demonstrated through both OSSEs and real-observation assimilation experiments.

2 | MODEL CONFIGURATION AND EXPERIMENTAL DESIGN

To test the new inflation algorithm, we design cycling data assimilation experiments using the ensemble Kalman filter (EnKF) data assimilation system developed at the Pennsylvania State University (PSU) (Zhang *et al.,* 2009; 2011; 2016; Weng and Zhang, 2012; 2016), which is built around the Advanced Research Weather Research and Forecasting model (WRF-ARW: Skamarock *et al.,* June 2008) version 3.6.1, and the Community Radiative Transfer Model (CRTM: Han *et al.,* 2006; 2007; Weng, 2007). For all experiments, we use three two-way nested domains for WRF simulations (with grid sizes of 27, 9 and 3 km). The WRF single-moment 6-class mixed-phase microphysics scheme (WSM6: Hong and Lim, 2006), the Yonsei University planetary boundary-layer scheme (Hong *et al.,* 2006), and the Rapid Radiative Transfer Model (RRTM) long-wave and short-wave radiation schemes (Iacono *et al.,* 2008) are applied for all domains. The cumulus parametrization scheme of Tiedtke (1989) is only applied to the coarsest (D1) domain. The BTs are simulated with the Successive Order of Interaction (SOI) forward solver (Heidinger *et al.*, 2006) with the OPTRAN code from CRTM. The standard profiles for the tropical region defaulted in CRTM are used above the model top.

For the assimilation strategy, we assimilate the BTs from one water vapour channel of GOES-16 ABI (channel 8: wavelength is 6.19 μm), which is sensitive to upper-tropospheric moisture content. BTs are assimilated with the successive covariance localization (SCL) method proposed by Zhang *et al.* (2009), which is designed to capture both convective-scale and large-scale structures with a combination of small and large covariance localization distances. Similar to Zhang *et al.* (2016) and Minamide and Zhang (2017), 30 km and 200 km localization radii are used for the observations thinned every 12×12 km and 18×18 km, respectively. No vertical covariance localization is used in this study. To account for large representativeness errors in assimilating all-sky BTs, we employ the Adaptive Observation Error Inflation (AOEI) method, whose effectiveness and justification for all-sky BT assimilation were explored in detail by Minamide and Zhang (2017). The AOEI method is designed to adaptively inflate the observation error variance when the squared innovation is greater than the combined variance of uninflated observational error variance and ensemble-estimated background error variance. For using both AOEI and ABEI, the observation error variance is likely to be further inflated with AOEI where innovation is large since the background variance may still be small after applying ABEI.

To derive the inflation magnitude and to explore the impacts of the new inflation method, we first conduct the perfect-model observing system simulation experiments (OSSEs) using the same 60 initial ensemble perturbations and the reference truth for Hurricane *Karl of 2010* as in the OSSE of Zhang *et al.* (2016) and Minamide and Zhang (2017), which is hereafter referred to as "Karl-OSSE". Both the ensemble and reference truth simulations use three two-way nested WRF domains with grid spacing of 27, 9 and 3 km that contain 199×149, 201×150, and 255×255 grid points, respectively. All model domains use 61 levels with the model top at 50 hPa in a stretched vertical grid. We compute the synthetic observations of the GOES-R ABI channel 8 (wavelength 6.19 μm) brightness temperature (BT) from the reference truth by adding random errors with a standard deviation of 3 K, which are assimilated hourly from 2200 UTC 16th to 2200 UTC 17 September 2010. Assimilated together is the tropical cyclone minimum sea-level pressure (SLP) observed at the simulated centre of the hurricane. All experiments employ the covariance relaxation to prior perturbation (RTPP) method of Zhang *et al.* (2004). Because the model error is not explicitly accounted for in this perfect-model OSSE framework, a relatively small value of 0.5 for the RTPP relaxation coefficient is applied for Karl-OSSE. A benchmark experiment only employs RTPP to maintain the ensemble spread, hereafter referred to as "CNTL". The second experiment employs the new ABEI method together with RTPP, hereafter referred to as "ABEI". ABEI will be compared to CNTL to highlight the potential impacts of the new inflation method.

Secondly, we conduct the observing system experiments (OSEs) that assimilates hourly the real-data observations of GOES-R ABI channel 8 BTs and the minimum SLP in the Tropical Cyclone Vital Database (TCvitals) at the estimated centre of Hurricane *Harvey of 2017* from 1200 UTC 23rd to 1200 UTC 24 August 2017 (this experimental framework is hereafter referred to as "Harvey-OSE"). For Harvey-OSE, we employ the model configurations similar to the PSU WRF-EnKF real-time Atlantic hurricane forecast and analysis system (Zhang *et al.,* 2009; 2011; Weng and Zhang, 2012; 2016). We used the three two-way-nested domains with horizontal grid spacings of 27, 9 and 3 km containing 378×243, 297×297, and 297×297 grids points, respectively. A moving nest strategy is used for the finer two domains (D2 and D3)

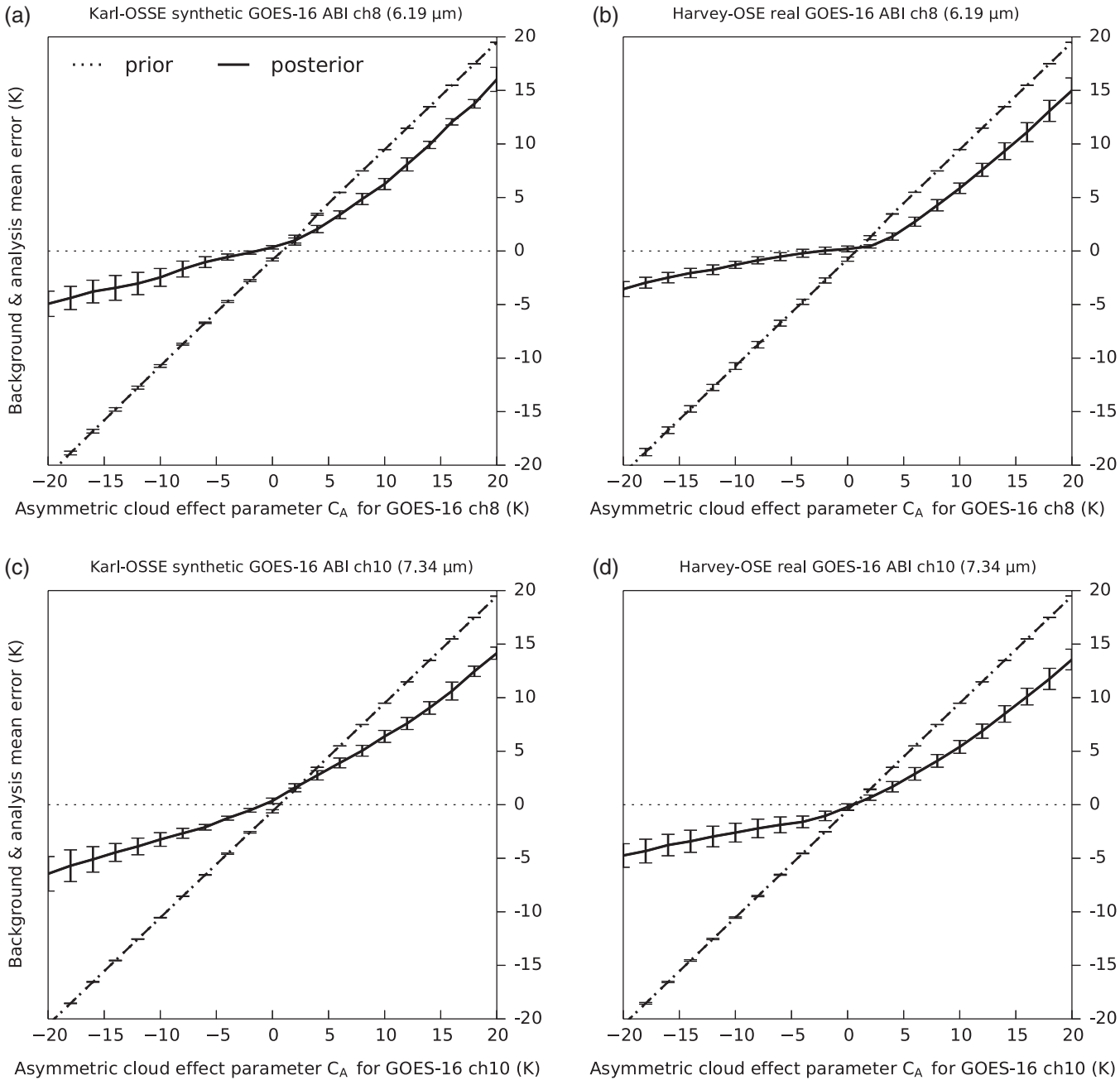

FIGURE 1 The prior and posterior biases of brightness temperatures of GOES-16 ABI (a,b) channel 8 and (c,d) channel 10 as a function of asymmetric cloud effect parameter C_A, with the standard deviation of the biases among different data assimilation cycles (error bar) from first 12 h of CNTL experiment of (a,c) Karl-OSSE and (b,d) Harvey-OSE

to follow the centre of the tropical cyclone vortex. All the domains use 41 vertical levels with the model top at 10 hPa in a stretched vertical grid; this new configuration is to be consistent with our real-time system instead of Karl-OSSE (we do not expect this will substantially affect the performance of ABEI). As in Karl-OSSE, the experiment that only applies RTPP is served as the benchmark, and the second experiment applies both RTPP and ABEI, which are again referred to as CNTL and ABEI, respectively. To account for the model error in the real-data applications, a larger RTPP coefficient of 0.75 is applied for Harvey-OSE, as is the default in the PSU WRF-EnKF real-time system (Weng and Zhang, 2016).

In addition to these two experiments, we also conducted another experiment using the covariance inflation method to adaptively estimate the multiplicative inflation factor proposed by Li *et al.* (2009) (hereafter referred to as "shACI" that represents the spatially homogeneous Adaptive Covariance Inflation). The shACI method calculates a domain-averaged multiplicative inflation factor at every assimilation cycle using the innovation statistics in the observation space. To alleviate the sampling error in estimating inflation factor from a limited number of observations, we further relax the current-cycle estimated inflation factor to that from the previous cycle with 37.5% from the current cycle and 62.5% from the previous cycle, following Li *et al.* (2009); the variance

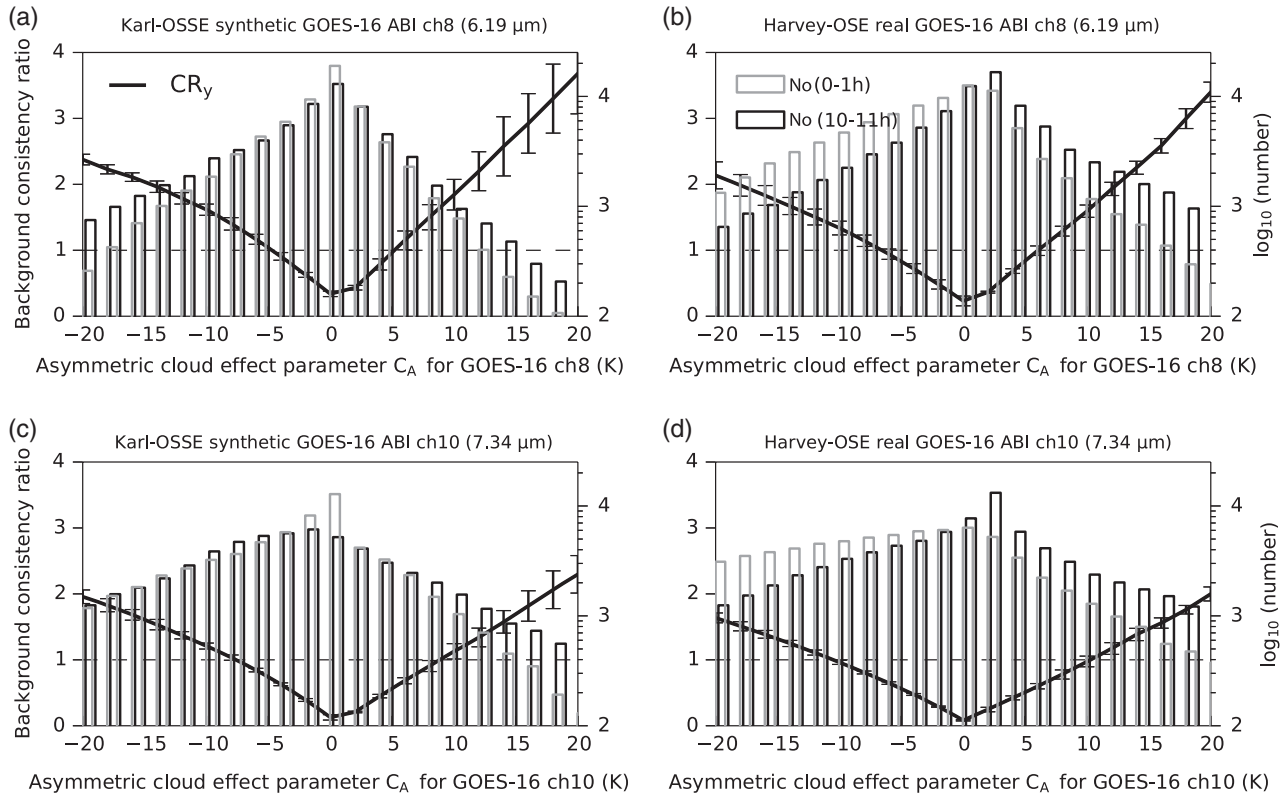

FIGURE 2 (Line-plot) The prior consistency ratio of brightness temperatures of GOES-16 ABI (a,b) channel 8 and (c,d) channel 10 as a function of the asymmetric cloud effect parameter C_A, with the standard deviation among different data assimilation cycles plotted as the error bar, from the first 12 h of assimilation experiments. (Bar-plot) The number counts of cloud scenes represented by the asymmetric cloud effect parameter C_A during 0–1 h versus 10–11 h. Plots are from CNTL experiments of (a,c) Karl-OSSE and (b,d) Harvey-OSE

of the estimated inflation factor in the current cycle is set to 1.0 as in Li *et al.* (2009) and the lower limit of the variance of the estimated inflation factor in the previous cycle is set as 0.6 similar to the fixed variance used in Gharamti (2018). We acknowledge that these values are empirical in nature, and may not necessarily be optimal for the case studied.

For Harvey-OSE, ABEI will be compared to CNTL and shACI to show the performance of the new inflation methodology with real-data all-sky radiance observations, as well as to highlight the difficulty in estimating the appropriate inflation factors in the model state space using the innovation statistic in the observation space with a highly nonlinear observation operator. In this study, the only difference among experiments CNTL, shACI and ABEI is their covariance inflation methodology, to highlight the effectiveness of using ABEI.

3 | THE ADAPTIVE BACKGROUND ERROR INFLATION (ABEI)

3.1 | Asymmetric cloud effect parameter

To examine how the filter performance and innovation statistics change among cloud scenarios, we utilize the cloud effect parameter introduced by Okamoto *et al.* (2014) that quantifies the impacts of cloud on BT value in infrared BT space, which was originally proposed in Geer and Bauer (2011) for microwave radiances. The cloud effect parameters for observation and EnKF prior are formulated as follows[2]:

$$C_O = |y_o - h_{clr}(\overline{x_b})|, \quad (1)$$

$$C_M = |h(\overline{x_b}) - h_{clr}(\overline{x_b})|, \quad (2)$$

where $h(\overline{x_b})$ is model prior simulated BT calculated from the EnKF prior mean $\overline{x_b}$, y_o is the observed BT, and $h_{clr}(\overline{x_b})$ is the model simulated prior BT without cloud-scattering and cloud-emission calculation as if clouds are removed. Both C_O and C_M increase with the presence of higher clouds, and approach zero in clear-sky regions. Following Geer and Bauer (2011) for microwave radiances, Okamoto *et al.* (2014) proposed to take an average of C_O and C_M to construct a "symmetric" cloud effect parameter for the infrared radiances which is neither biased toward the observation-based nor the model-based evaluation.

The purpose of the current study is to evaluate the "cloud-scene-dependent" background error inflation, in particular with regard to the impacts of match/mismatch between

[2]To be consistent with definition in the original Okamoto *et al.* (2014) paper, we used the absolute difference to calculate the cloud effect parameter C_O and C_M in this study. However, practically in the vast majority of cases, $h_{clr}(\overline{x_b})$ is greater than y_o and $h(\overline{x_b})$. Thus, the calculations of C_O and C_M are approximately the same as if simply subtracting y_o or $h(\overline{x_b})$ from $h_{clr}(\overline{x_b})$, and the asymmetric cloud effect parameter C_A is almost identical to the B-O innovation, as shown in Figure 1.

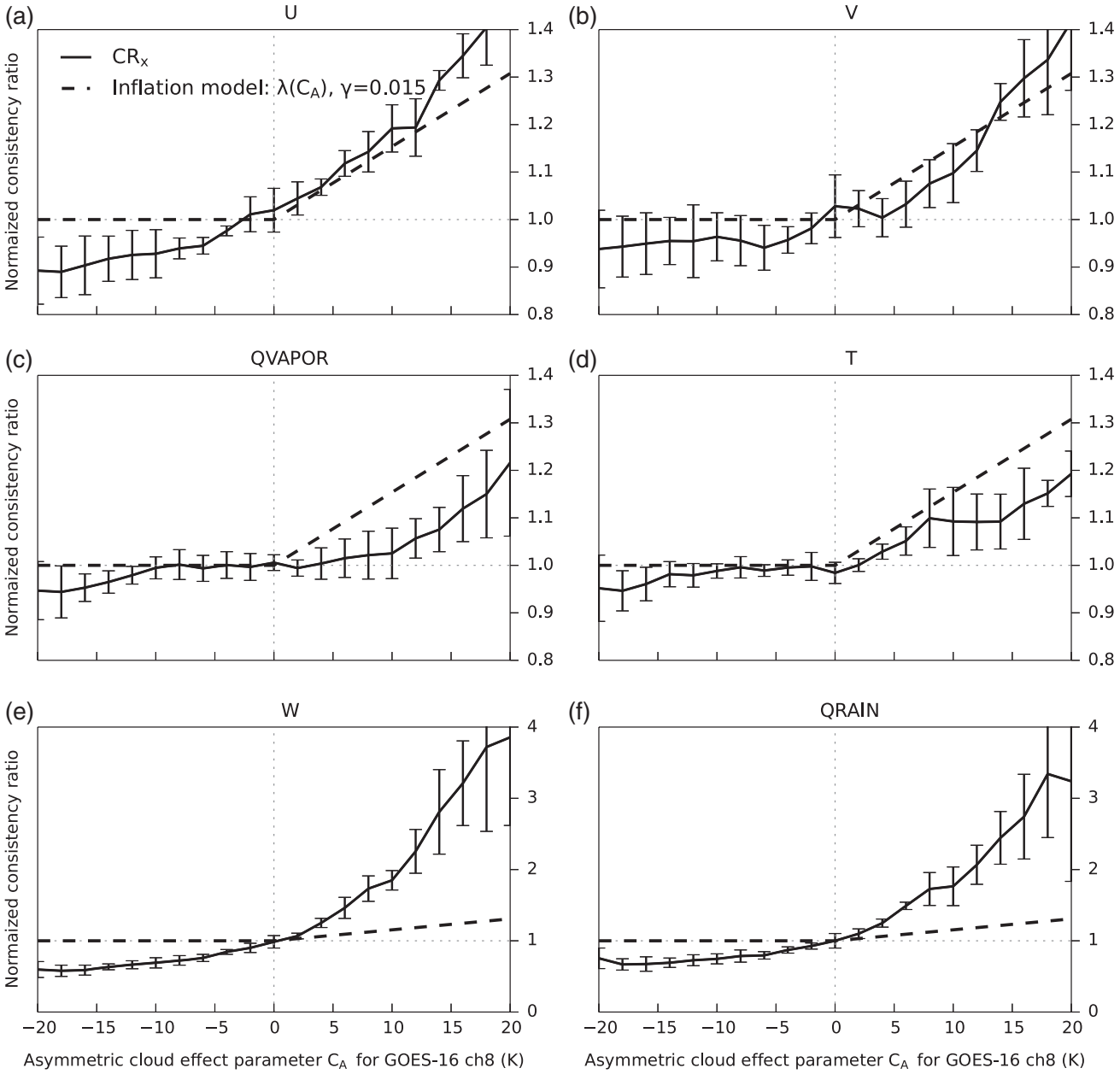

FIGURE 3 The prior consistency ratio of (a) zonal wind, (b) meridional wind, (c) atmospheric water vapour mixing ratio, (d) temperature, (e) vertical wind and (f) liquid rain hydrometeors as a function of the asymmetric cloud effect parameter C_A, normalized by the domain-averaged consistency ratio at the corresponding time calculated from the CNTL experiment of Karl-OSSE, with the standard deviation plotted as the error bar. The dashed-line represents the linear inflation factor coefficient used in this study

observation and model on the bias, filter performance and innovation statistics. Here we define an "asymmetric" cloud effect parameter, C_A, by taking the difference between them:

$$C_A = C_O - C_M. \tag{3}$$

When C_A is close to zero, the cloud scene matches well between the model and observation (i.e. either both clear, or both cloudy with similar cloud height). C_A becomes positive when cloudy-sky is observed but clear-sky is modelled, and negative when clear-sky is observed but cloudy-sky is modelled. This formulation allows us to quantify the degree of mismatch of cloud patterns by a continuous parameter. We use this asymmetric cloud effect parameter, C_A, as a predictor for the following adaptive inflation strategy. Because the prior mean remains unchanged both in model and observation spaces after applying the inflation in this study, the usage of asymmetric cloud effect parameter does not directly change the innovation statistics (histogram).

3.2 | Cloud-scene-dependency of innovation statistics

To show the cloud-scene dependency of filter performance, we firstly compare the bias of the EnKF prior and posterior for GOES-R ABI channel-8 and channel-10 brightness temperatures as a function of C_A from the CNTL experiment of Karl-OSSE and Harvey-OSE (Figure 1). In addition to the assimilated channel 8, we also show channel 10 (wavelength 7.34 μm), which is not assimilated but sensitive to the

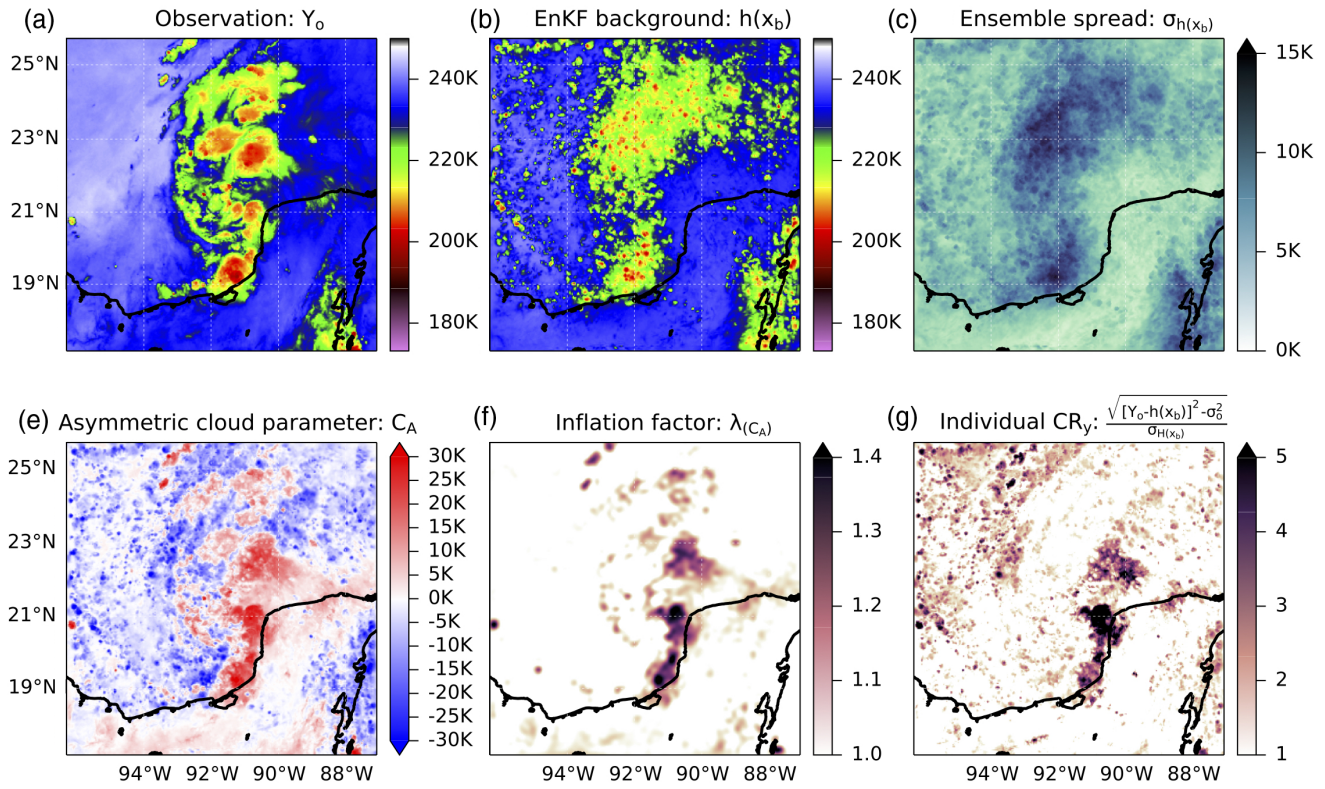

FIGURE 4 The spatial distribution of (a) GOES-16 observation, (b) EnKF prior mean, (c) ensemble prior standard deviation, (d) asymmetric cloud effect parameter C_A, (e) calculated cloud-scene-dependent multiplicative inflation factor, and (f) the ratio between the absolute difference between the observation and prior estimate and ensemble standard deviation. All figures are for brightness temperature channel 8 verified at 1200 UTC 23 August 2017. The ensemble priors are from ABEI experiment of Harvey-OSE [Colour figure can be viewed at wileyonlinelibrary.com].

moisture content at different heights, as independent verifications. By design of the asymmetric cloud effect parameter C_A, the prior bias (dashed line in Figure 1) almost perfectly corresponds to C_A for both channels 8 and 10 in both Karl-OSSE and Harvey-OSE. When the filter properly reduces the prior error, the posterior bias (solid line in Figure 1) approaches closer to zero than the corresponding prior bias. For negative C_A, the negative prior biases are effectively corrected by the filter in which the spuriously prior-estimated clouds can be mostly removed, resulting in a much-reduced posterior bias.

However, the improvements are severely limited for the positive C_A. The posterior bias curve in positive C_A is approximately parallel to those of the prior, and deviates farther away from zero with increased values of C_A. Physically, fixing the negative bias in negative C_A scene amounts to removing spuriously modelled or overestimated clouds, while fixing the positive bias in positive C_A scene represents the development of clouds in spurious clear-sky or underestimated cloudy-sky regions. Figure 1 is consistent with an early study of Vukicevic *et al.* (2004) that reported the difficulty of developing clouds in spuriously modelled clear-sky regions compared to removing spuriously modelled clouds.

To investigate the source of this asymmetry, we calculate the consistency ratio (CR) in the BT observation space as a function of C_A (Figure 2). Here, CR is defined as the ratio of the square-root of the subset-averaged squared error (i.e. root mean square error or RMSE) over the square-root of the subset-averaged ensemble variance. Choice of subset can be arbitrary, but we want it to consist of samples that share the same cloud scene. In this study, domain 3 of the CNTL experiments from Karl-OSSE is divided into bins with a 2 K C_A interval. Each bin is composed of one subset, and CRs are calculated for each subset independently. CR in the observation space (referred to as CR_y) can be formulated as follows for any subset:

$$CR_y = \begin{cases} \dfrac{\sqrt{\frac{1}{S_n}\sum_{s=1}^{S_n}\{y_{o,s}-h(\overline{x_{b,s}})\}^2-\sigma_o^2}}{\sqrt{\frac{1}{S_n}\sum_{s=1}^{S_n}\sigma_{h(x_{b,s})}{}^2}}, & \text{(for OSEs)} \\ \dfrac{\sqrt{\frac{1}{S_n}\sum_{s=1}^{S_n}\{h(x_{t,s})-h(\overline{x_{b,s}})\}^2}}{\sqrt{\frac{1}{S_n}\sum_{s=1}^{S_n}\sigma_{h(x_{b,s})}{}^2}}, & \text{(for perfect} - \text{model OSSEs)} \end{cases} \quad (4)$$

where h is the observation operator, x is the model state variables, y is the observed variables, subscripts o, t, b are observation, truth and EnKF prior, respectively, $\sigma_{y_b}(=\sigma_{h(x_b)})$ is the prior ensemble standard deviation in the observation space from the mean of ensemble members in the observation space, σ_o is the observation error standard deviation and S_n is the number of the state variables classified for a particular subset. Because perfect observations (i.e. observations without observation errors) can be obtained in perfect-model OSSEs, the formulations are different between OSEs and OSSEs. Ideally, CR should be designed for the ensemble spread to accurately represent the prior error. The CR value becomes smaller than one with an over-dispersive situation,

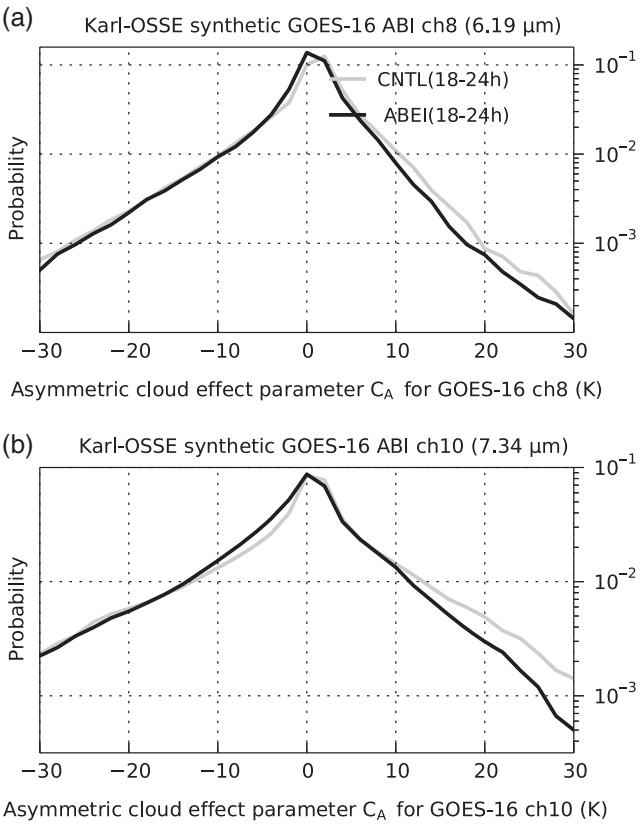

FIGURE 5 Probability distribution functions (PDF) of cloud scenes represented by the asymmetric cloud effect parameter C_A during the 18 to 24 h assimilation cycles from the experiments of Karl-OSSE for CNTL versus ABEI. (a) Channel 8, (b) channel 10

while larger than one with an under-dispersive situation. If CR is larger than one, the filter over-trusts the background estimation, reduces the analysis increments and analyses the posteriors with larger errors than the theoretical expectations, which could lead to filter divergence.

Figure 2 shows CR calculated with a constant of 3 K as σ_o. For both channels 8 and 10, and both for Karl-OSSE and Harvey-OSE, CR_y increases as C_A deviates from zero (Figure 2), even for negative C_A whose prior bias can be better corrected by the filter (Figure 1). The ensemble has larger spread than RMSE only around $-6\ \text{K} \le C_A \le 6\ \text{K}$ for channel 8, and $-10\ \text{K} \le C_A \le 10\ \text{K}$ for channel 10 in the observation space, which indicates that these experiments may suffer from a severely under-dispersive ensemble in large portions of the domain. The asymmetry between negative and positive C_A also exists in CR_y. For positive C_A, CR_y deviates from 1.0 more rapidly than in negative C_A. CR_y values reach as high as 3.7 for channel 8 with $C_A = 20$ K, which means the prior error is larger than that estimated by the ensemble spread by a factor of 3.7, which highlights the difficulty in keeping the appropriate amount of background spread through assimilating observations with a nonlinear observation operator. These high CR_y values will be further discussed later in this section, together with CR in the model state space.

Despite the large temporal variability of domain-averaged CR_y (which will be shown in section 4 with Figures 7 and 12), CR_y values at each C_A scene do not vary considerably during data assimilation cycles as shown as the error bar in Figure 2. Note that the temporal variance of CR_y from Karl-OSSE is relatively larger than Harvey-OSE, likely because of its smaller sample size. Due to smaller model error in perfect-model OSSEs, the occurrence of extreme C_A scenes is much less frequent, which in turn results in noisier CR lines. For example, the CR_y values for channel 8 in the real-data experiment for *Harvey* are often around 3.3 at $C_A = 20$ K (Figure 2b). Rather, the time dependency can be seen in their number distribution. The bar plot in Figure 2 shows that the occurrence of positive (and negative, too, for channel 8) C_A becomes more frequent in later assimilation cycles. The increase of high (or low) C_A regions with large CR_y will potentially cause filter divergence and degrade the overall filter performance. Furthermore, given that the asymmetry of posterior bias, asymmetric increase of positive or negative C_A scenarios may also serve as a source of overall bias. The CR_y curves from Karl-OSSE are noisier than from Harvey-OSE, in particular in positive C_A, but they overall show consistent features. Thus, Figures 1 and 2 indicate that the innovation statistics, such as the prior and posterior bias and the consistency ratio, for each C_A scene are relatively constant among assimilation cycles, but their distribution of occurrence changes, which might potentially introduce bias or cause filter divergence.

Taking the advantage of the truth run in the OSSE framework, Figure 3 compares CR as a function of C_A similarly to Figure 2 but for the model state variables normalized by the domain-averaged CR at the corresponding time to illustrate the different behaviours of CRs among various C_A scenes (hereafter, CRs in the model state space are referred to as CR_x). All state variables in Figure 3 show a clear asymmetric pattern that consistently exists during the entire data assimilation cycle despite considerable temporal variability in the domain-averaged CRs (which will be discussed in detail in section 4). CR_x is slightly smaller than or around one in negative C_A, but significantly larger than one in positive C_A for all state variables, which is different from CR_y. This asymmetry of CR_x can explain the asymmetric filter performance shown in Figure 1. Because we update the state variables by the EnKF, the prior bias in negative C_A can be fixed relatively easily because the state variables have enough spread to cover the error. Meanwhile, the filter faces more difficulty in correcting the positive prior bias in positive C_A, because most of the state variables are under-dispersive in this scene. Although the CR_x curves follow the similar asymmetric pattern for all state variables, the magnitude varies among different state variables depending on their respective sensitivities to BT calculation. Most of the CR_x of dynamic and thermodynamic model state variables including zonal and meridional wind, moisture and temperature range around 1.0–1.8 at $C_A = 20$ K (Figure 3a–d), while they reach as high as 3–4 for vertical wind and hydrometeors, which is the same order as CR_y (Figure 3e–f). Comparing Figures 2 and

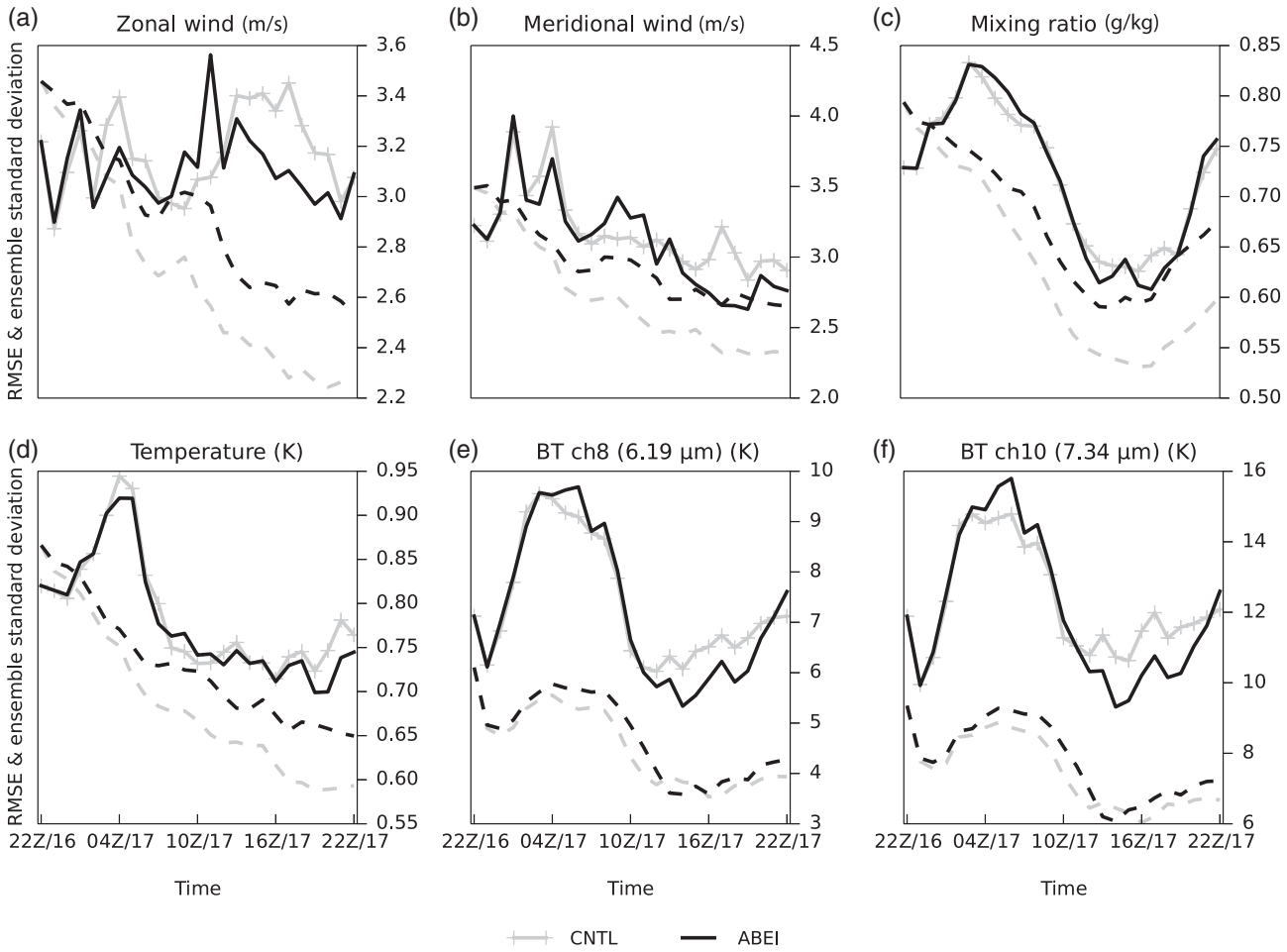

FIGURE 6 Temporal evolution (2200 UTC 16th–2200 UTC 17 September 2017) of domain-averaged EnKF background RMSEs (solid) and standard deviations (dashed) from CNTL (grey) and ABEI (black) for (a) zonal wind, (b) meridional wind, (c) atmospheric water vapour mixing ratio, (d) temperature, (e) brightness temperatures of GOES-16 ABI channel 8 and (f) channel 10,

3, CRs are shown to act differently in observation space and model state space. In positive C_A, CR_y is similar to CR_x of vertical wind and hydrometeors, which are the model state variables directly and indirectly sensitive to radiative transfer simulations through convective activity, but is greatly exaggerated compared to other state variables. For C_A close to zero, CR_y is much smaller than one, but CR_x of most of the state variables is around one. In negative C_A, the CR_y is larger than one, which indicates under-dispersive, while CR_x is mostly around or slightly smaller than one, which indicates marginally over-dispersive situations. Thus, for radiance assimilation, diagnosing the innovation statistics only in the observation space and directly applying them into the model state space (such as in estimating the multiplicative covariance inflation) may potentially cause severe filter deficiency.

3.3 | Cloud-scene-dependent empirical formulation of ABEI

The small variability of CR_x among different assimilation cycles at each C_A scene indicates the potential in using C_A as a predictor for the multiplicative covariance inflation factor. Multiplicative inflation is a method to linearly increase the distance (ensemble perturbation) between the EnKF prior mean and each ensemble member for the kth state variable (for $k = 1, 2, 3, \ldots, K$; K is the dimension of the state vector):

$$x'_{k,\mathrm{new}} = \lambda_k x'_k, \tag{5}$$

where $\bar{x}$ and x' represent EnKF prior mean and perturbation, respectively. The degree of inflation is controlled by the inflation factor, denoted as λ. Following the well-established innovation diagnosis (Parrish and Derber, 1992; Dee, 1995; Desroziers *et al.,* 2005), the expected innovation statistics satisfy the following equation:

$$\langle \boldsymbol{d}, \boldsymbol{d}^{\mathrm{T}} \rangle = \langle [\boldsymbol{h}(\overline{\boldsymbol{x}_\mathbf{b}} + \boldsymbol{x}'_{\mathbf{b},\mathbf{new}}) - \boldsymbol{h}(\overline{\boldsymbol{x}_\mathbf{b}})] [\boldsymbol{h}(\overline{\boldsymbol{x}_\mathbf{b}} + \boldsymbol{x}'_{\mathbf{b},\mathbf{new}}) - \boldsymbol{h}(\overline{\boldsymbol{x}_\mathbf{b}})]^{\mathrm{T}} \rangle + \boldsymbol{R}, \tag{6}$$

where $\boldsymbol{d}$ denotes the innovation vector (i.e. the first-guess departure), $\boldsymbol{R}$ the observation error, and pointy brackets the expectation operator. Thus, the value of λ is calculated to satisfy this equation. In the framework of perfect-model OSSEs where the observation operator is assumed as the identity matrix, we can directly estimate λ, which corresponds to CR_x for the sth state variable ($s = 1, 2, 3, \ldots, S_n$; S_n is the total number of the state variables classified into a particular subset) by averaging the diagonal terms of Equation 6 under

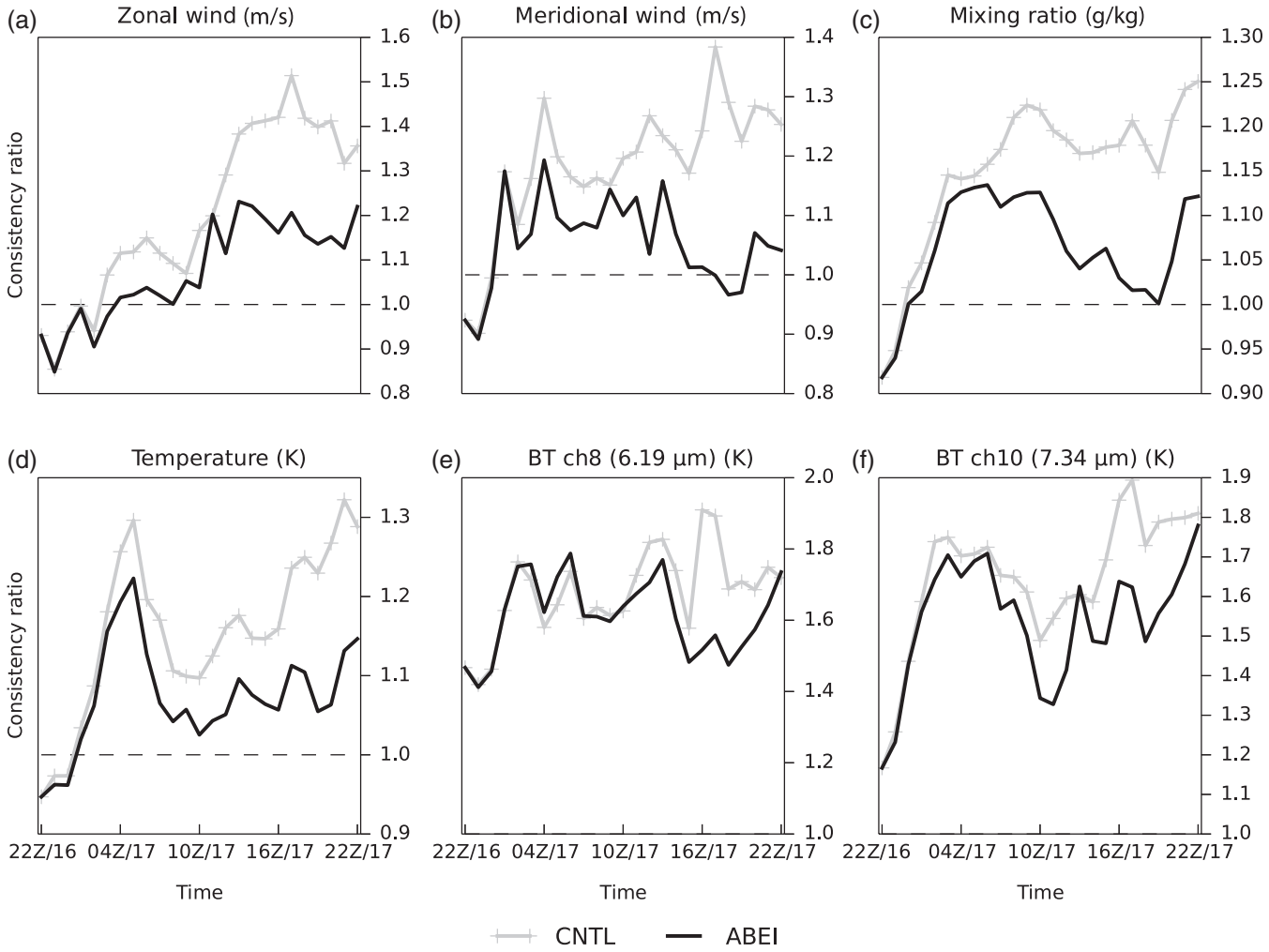

FIGURE 7 As in Figure 6 but for the consistency ratio

the assumption that the state variables in a particular subset share the same innovation statistics:

$$\frac{1}{S_n}\sum_{s=1}^{S_n}(x_{\mathrm{t,s}}-\overline{x_{\mathrm{b,s}}})^2=\frac{1}{S_n}\sum_{s=1}^{S_n}\langle\lambda\rangle^2{\sigma_{x_{\mathrm{b,s}}}}^2+0,$$

$$\langle\lambda\rangle^2=\frac{\sum_{i=1}^{S_n}(x_{\mathrm{t,s}}-\overline{x_{\mathrm{b,s}}})^2}{\sum_{i=1}^{S_n}{\sigma_{x_{\mathrm{b,s}}}}^2}={CR_x}^2. \tag{7}$$

Using the normalized ${CR_x}^2$ values, i.e. ${CR_x}^2$ defined in Equation 7 divided by domain-averaged ${CR_x}^2$ as shown in Figure 3, we formulate the spatial variations of inflation factors as a function of C_A by a linear model as shown as the dashed black line in Figure 3, for simplicity and easiness of implementation:

$$\lambda_{(C_A)}=\begin{cases}\lambda_{\max}, & \text{if } \frac{\lambda_{\max}-1}{\gamma}\le C_\mathrm{A}\\ \gamma C_A+1, & \text{if } 0\le C_\mathrm{A}\le\frac{\lambda_{\max}-1}{\gamma}\\ 1, & \text{if } C_\mathrm{A}\le 0.\end{cases} \tag{8}$$

The γ value controls the increase of $\lambda_{(C_\mathrm{A})}$ with positive C_A, which may or may not vary among the state variables. This formulation keeps the ensemble spread unchanged for negative C_A, while the inflation factor increases linearly with positive C_A. To avoid assigning too large inflation factors, the maximum value ($\lambda_{\max}$) is set to be 1.4 in this study. Note that by using the normalized ${CR_x}^2$ values for the formulation, ABEI is designed to allow simultaneous application of other covariance inflation methods, such as RTPP in this study, or any other adaptive inflation methods that further control the domain-averaged ${CR_x}^2$. Because the CR_x values are similar among the state variables of horizontal wind, moisture and temperature, whose initializations are known to have larger impacts on forecast than those of vertical wind or hydrometeors, we apply the same γ for all state variables, which may help to lessen the degree of dynamical imbalance in the cloud-scene-dependent inflation. The values of γ is derived from calculating the slope of linear regression line in positive C_A for horizontal wind components, moisture and temperature fields (i.e. state variables in Figure 3a–d). Because we use C_A as a predictor to estimate how much the state variables are constrained by assimilating a particular observation network, we expect the values of γ to mainly depend on the sensors and the observation network, together with model configurations. For example, in this study which assimilates all-sky infrared BTs and minimum SLP, the calculated values of γ are 0.015, 0.012 and 0.009 for the GOES-16 ABI channel 8, 9 and 10, respectively. Because the original cloud parameter (Okamoto *et al.*, 2014) was designed for the global

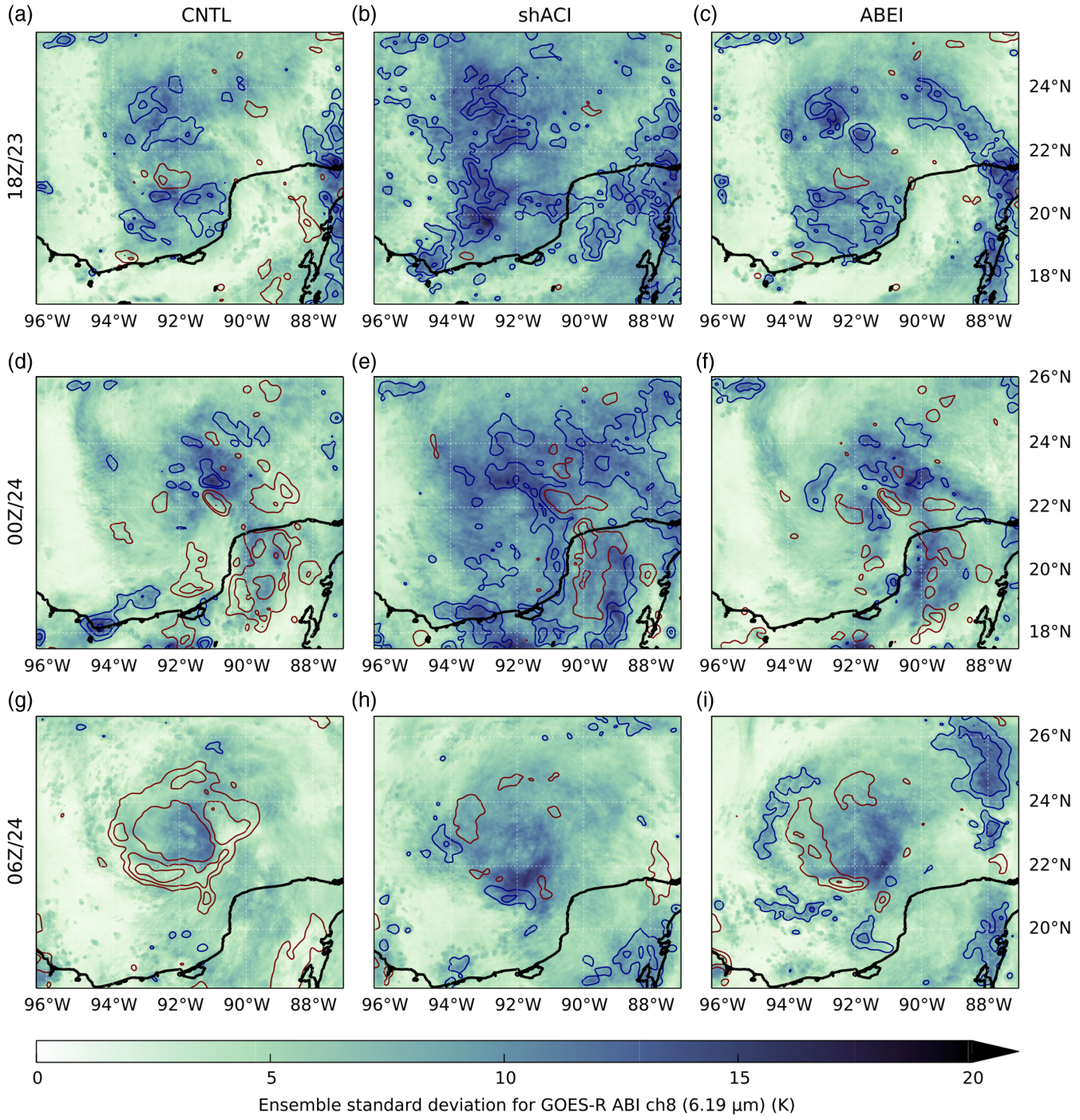

FIGURE 8 The ensemble standard deviation of simulated brightness temperatures of GOES-16 ABI channel 8 (colour-shaded) and asymmetric cloud effect parameter C_A (contoured with red lines for positive values and blue lines for negative values, every 10 K) at (a–c) 1800 UTC 23rd (after 6 h assimilation cycle), (d–f) 0000 UTC 24th and (g–i) 0600 UTC 24 August 2017 from the (a,d,g) CNTL, (b,e,h) shACI and (c,f,i) ABEI experiment of Harvey-OSE [Colour figure can be viewed at wileyonlinelibrary.com].

application, we expect the values of γ to be the same globally, the applicability of which would be further investigated in future studies. We further spatially smooth the inflation factors by using the localization function to suppress the model imbalance and adjustment as suggested by Anderson (2009).

The ensemble filter algorithm with spatially varying ABEI proceeds as follows:

1. The prior ensemble estimates are averaged to calculate the ensemble prior mean.
2. The first estimation of the multiplicative inflation factor (referred to as λ) is set as one.
3. The multiplicative inflation factor field λ is serially updated by processing each radiance observation $y_{o,i}$ (for $i = 1, 2, 3, \ldots, p$; p is the number of radiance observations):

3.i. calculate the corresponding asymmetric cloud effect parameter $C_{A,i}$, using the observation and ensemble prior mean;

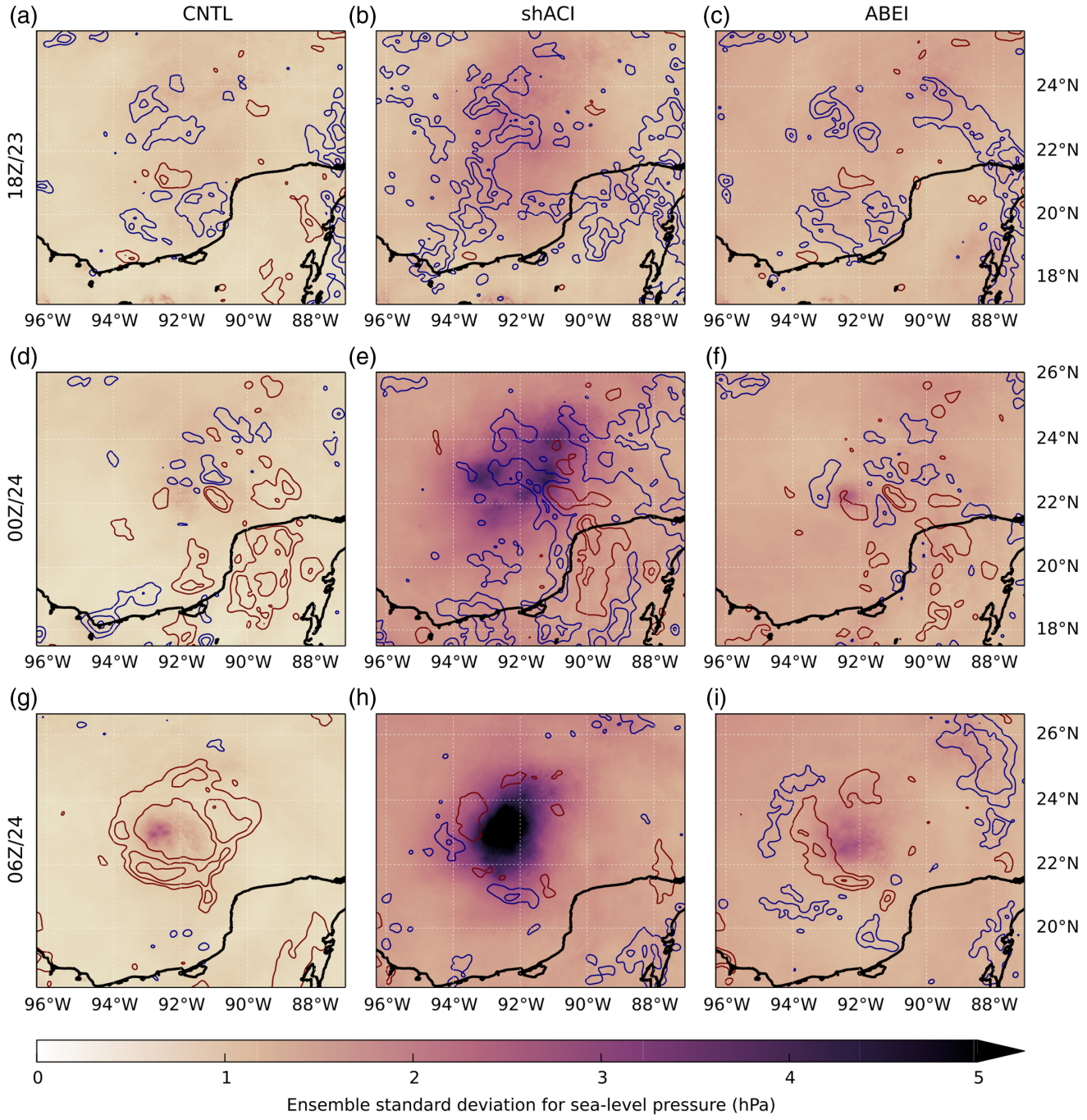

FIGURE 9 As in Figure 8 but for the ensemble standard deviation of sea-level pressure (colour-shaded) [Colour figure can be viewed at wileyonlinelibrary.com].

3.ii. obtain the empirical multiplicative inflation factor $\lambda_{(C_{A,i})}$, using Equation 8;

3.iii. assume that the correlation of inflation parameters has the same structures as the localization function for the corresponding state variables:

$$\mathrm{corr}(\lambda_k, H_i\lambda) = \rho_{k,i}, \tag{9}$$

where $\rho_{k,i}$ is the same localization function as what will be used to update the state vector element k by observation $y_{o,i}$ in step Equation 5 of the EnKF analysis, H_i is the interpolating semi-observation operator that maps λ defined on the state space to the locations of $y_{o,i}$;

3.iv. update the "observed" multiplicative inflation factor field:

$$\lambda_{k,\mathrm{new}} = \lambda_k + \rho_{k,i}[\lambda_{(C_{A,i})} - H_i\lambda] \tag{10}$$

As defined in step (2), initially, $\lambda = 1$ (i.e. $\lambda_k^o = 1$ for $k = 1, 2, 3, \ldots, K$; K is the dimension of state vectors). λ is serially updated through processing each observation. Thus, $\lambda_{k,\mathrm{new}}$ updated by ith observation will be served as the λ_k for $(i+1)$th observation.

4. Inflate the prior ensemble for each state vector component by the corresponding multiplicative inflation factor:

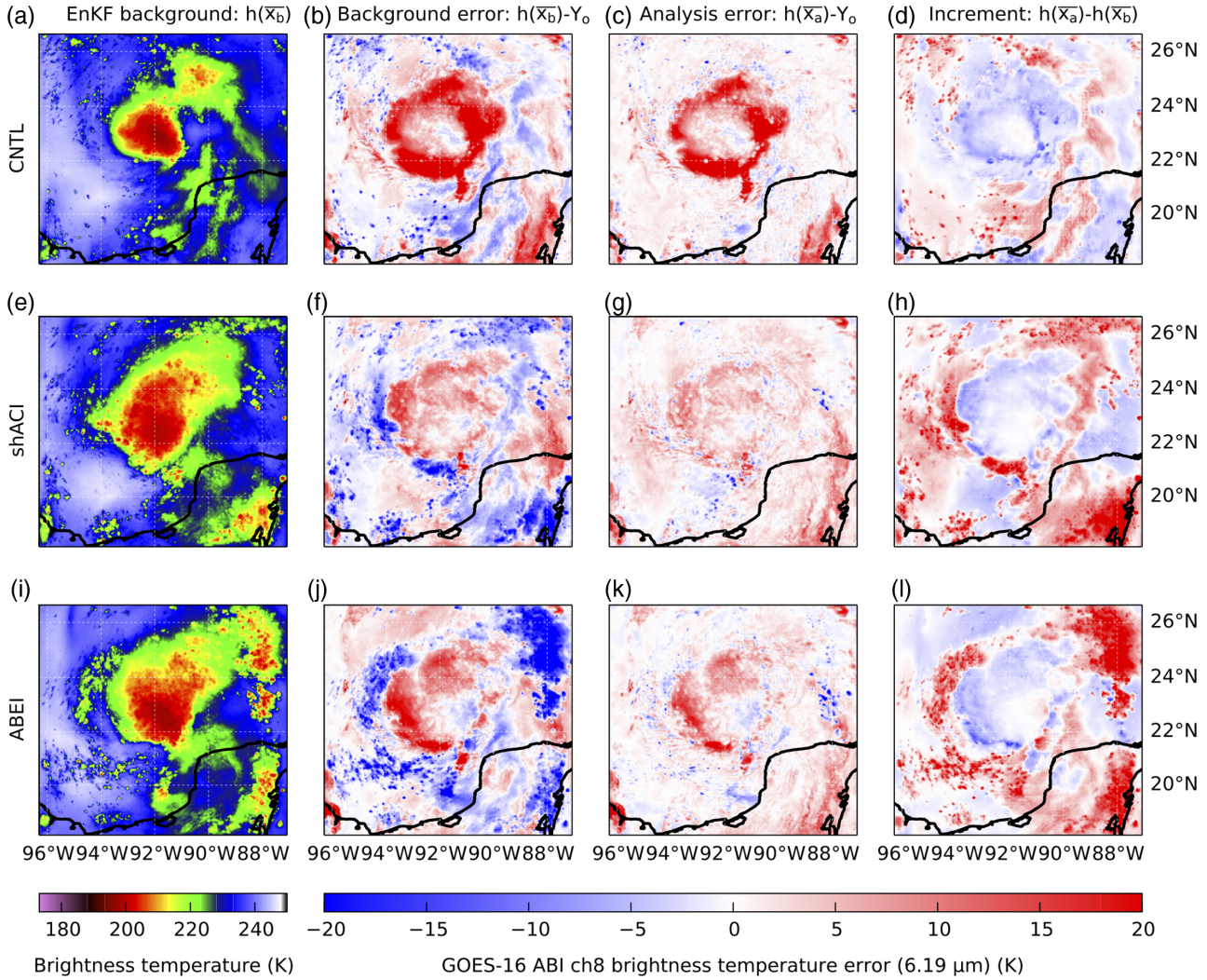

FIGURE 10 The simulated brightness temperature for GOES-16 ABI channel 8 of (a,e,i) EnKF prior mean, (b,f,j) EnKF prior mean error, (c,g,k) EnKF posterior mean error and (d,h,l) EnKF mean analysis increment, from (a–d) CNTL, (e–h) shACI and (i–l) ABEI experiment of Harvey-OSE, verified at 0600 UTC 24 August 2017 [Colour figure can be viewed at wileyonlinelibrary.com].

$$x'_{\mathrm{b},k,\mathrm{inf}} = \lambda_k x'_{\mathrm{b},k}. \tag{11}$$

5. Complete the EnKF analysis update for the state vector with the observations at this time.

Figure 4 exemplifies the spatially varying inflation factor field from Harvey-OSE prior at the initial assimilation cycle. The EnKF background mean estimate roughly captures the distribution of convective activity over the Gulf of Mexico associated with a large prior ensemble spread, but the prior estimate does not capture the strong convection along the northwest coastline of the Yucatan Peninsula, nor over the Gulf of Mexico located around 90.5°W, 22.5°N (Figure 4a–c). Reflecting the scene in which clear sky is incorrectly estimated by the prior ensemble mean while the observations indicate the cloudy conditions, C_A becomes positive in the corresponding regions (Figure 4d), for which the multiplicative inflation factors will be applied (Figure 4e). Figure 4f shows the distribution of individual CR_y (i.e. $(\sqrt{(y_0 - h(x_\mathrm{b}))^2 - \sigma_\mathrm{o}^2})/\sigma_{h(x_\mathrm{b})}$) if it were to be calculated independently for each grid. Consistent with Figure 2, CR_y are greater than one in both positive and negative C_A regions. The proposed ABEI method will inflate the regions with the lack of observed convection (i.e. with a positive C_A). This is one of the advantages of using an off-line method to calculate the inflation factors instead of estimating them individually for each observation in the observation space, because CR_y is largely exaggerated from CR_x in the negative C_A regions likely due to the strong nonlinearity in the observation operator. Note that ABEI is designed to improve the innovation statistics in the model state space and not always in the observation space, so that large CR_y values may still exist after applying ABEI. Thus, we will benefit from the simultaneous usage of ABEI and heteroscedastic modelling of observation error inflation, such as AOEI, by alleviating the different innovation statistics in model state and observation spaces. Another advantage of using the empirically derived inflation factors through ABEI is its ability to keep the negative C_A regions uninflated (without being contaminated by high CR_y values). The clear-sky

scenario that is inaccurately estimated in the observed cloudy regions is shown to be under-dispersive only in the radiance observation space (Figure 2) and not in the model state space (Figure 3). These snapshots exhibit the potential of our empirical ABEI method to calculate cloud-scene-sensitive multiplicative inflation factors which can better detect the under-dispersive regions without unnecessary inflation.

4 | POTENTIAL IMPACTS OF ABEI

4.1 | Observing system simulation experiment: Hurricane *Karl of 2010*

We first compare the performance of ABEI in Karl-OSSE. Figure 5 compares the distribution of C_A between CNTL with and without application of ABEI. According to Figure 2, which indicated that the under-dispersive ensemble is caused by the transition to high or low C_A scene rather than the change of CR within each C_A, Figure 5 compares the probability distribution with respect to C_A among the experiments. For both channels 8 and 10, ABEI decreases the occurrence of positive C_A scenes compared to CNTL after 18 cycles of hourly EnKF assimilation, which indicates that ABEI is able to maintain the ensemble spread to avoid severe mismatched scenes where the observed cloudy region is inaccurately estimated by the ensemble mean prior as clear sky. The distribution patterns in negative C_A are similar between CNTL and ABEI, because ABEI does not perform any additional inflation with negative C_A. Since there is an asymmetry in the performance (i.e. reduction of the error), the increased asymmetry of C_A scenes contributed to reducing the overall bias (not shown).

Figure 6 compares the temporal evolution of the square root of domain-averaged square error (as known as root mean square error, or RMSE) of the prior and EnKF analysis, and square root of domain-averaged ensemble variance of the EnKF prior for selected variables. The differences in RMSEs are small between CNTL and ABEI for the first 12 h, but the RMSEs of ABEI starts to become slightly smaller than CNTL after around 12 h, in particular for the wind and BT fields. Although overall difference in RMSEs is small between CNTL and ABEI, the ensemble spread clearly exhibits the advantage of using ABEI. For all state variables and BTs, the ABEI experiment shows a larger ensemble spread that is closer to the corresponding RMSE. The temporal evolutions of CRs are shown in Figure 7. For the meridional wind and mixing ratio, ABEI is able to maintain the CR around 1.0 after 12 h of assimilation, while CR of CNTL keeps increasing (Figure 7b,c). For the zonal wind and temperature, CR is marginally higher than 1.0, staying around 1.1–1.2, but again significantly smaller than CNTL (Figure 7a,d). ABEI is also able to maintain CR of BTs slightly smaller than CNTL (Figure 7e,f), but those CR_y values are around 1.4–1.6, which are much larger than other state variables. This is consistent with our findings in the previous section that the CR in the

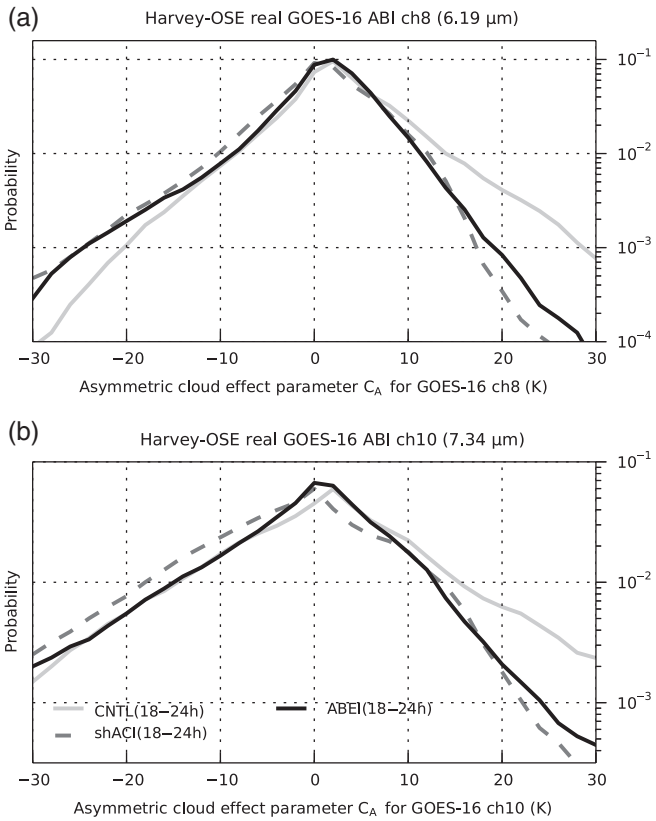

FIGURE 11 As in Figure 5, but for Harvey-OSE

radiance observation space may be exaggerated compared to CR in the model state space. Worth noting is that the filter performances at each C_A scene shown in Figures 1 and 2 (i.e. the prior and posterior bias and the consistency ratio) do not change by using ABEI (not shown), but the changes in the distribution of the occurrence of each C_A scene (Figure 5) improve the CR and RMSEs. These results indicate that, although the CR_y itself does not always correspond to CR_x, ABEI that empirically connects the observed BT and CR_x can contribute to maintaining the ensemble spread at a more desirable value (closer to 1.0).

4.2 | Real-data GOES-R observation assimilating experiment: Hurricane *Harvey of 2017*

Given the promising performance of ABEI in Karl-OSSE, we further investigate the potentials of ABEI for analysing and forecasting Hurricane *Harvey of 2017* by applying it with real-data all-sky radiance observations from GOES-R. In addition to CNTL and ABEI experiments as in Karl-OSSE, we conduct an additional experiment that adaptively estimates a spatially homogeneous inflation factor in the observation space, referred to as "shACI", to exemplify the potential issues in estimating proper inflation factors from only the innovation statistics in the observation space.

Figure 8 exhibits the temporal evolution of the spatial distribution of C_A and BT ensemble spread. At 1800 UTC 23 August 2017, after 6 hourly assimilation cycles, both CNTL and ABEI have similarly large ensemble spread of BTs over

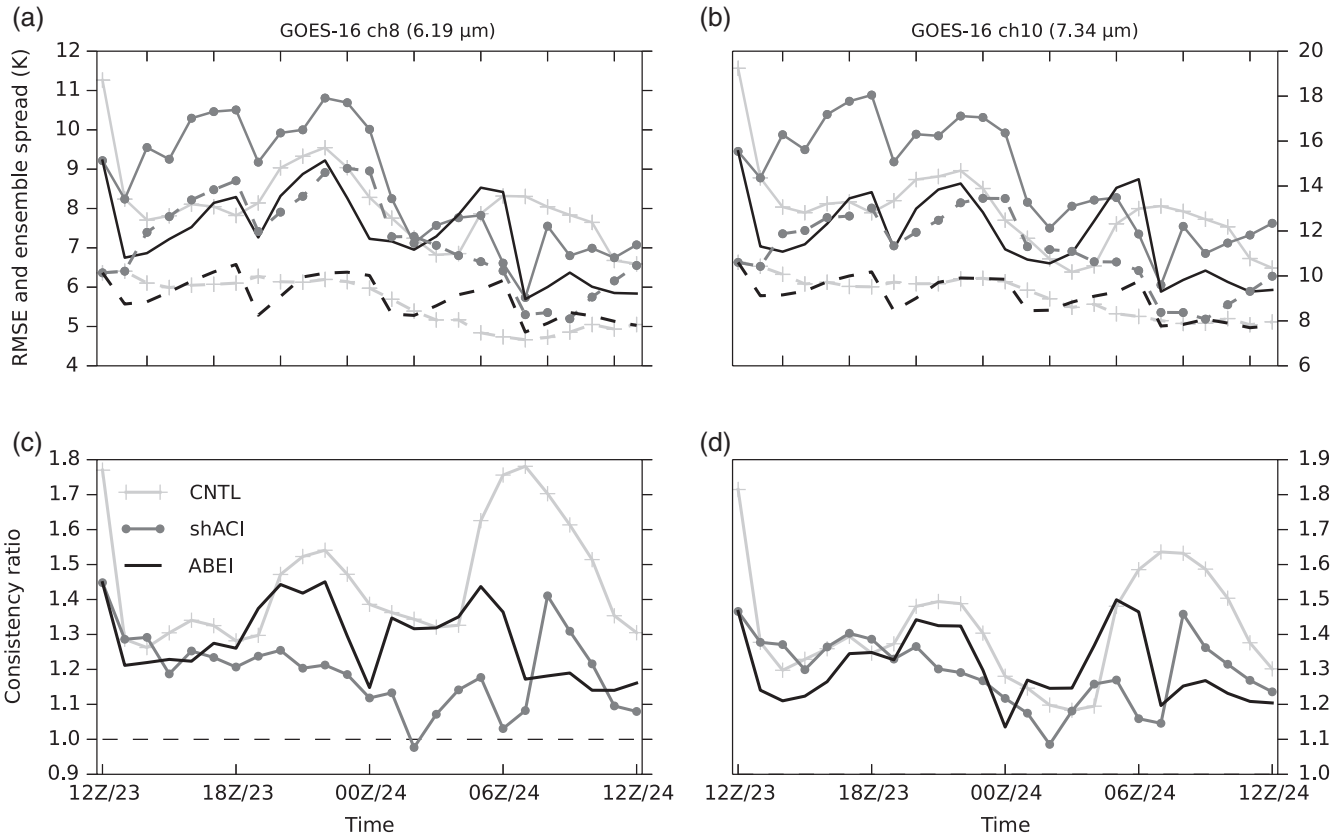

FIGURE 12 (a,b) As in Figure 6e,f, and (c,d) as in Figure 7e,f, but for Harvey-OSE

the Gulf of Mexico with both positive and negative C_A values (Figure 8a,c). After 12 and 18 h of assimilation, ABEI is able to better analyse a smaller area of negative C_A, which is shown to be under-dispersive, than CNTL in particular over the Yucatan Peninsula at 0000 UTC 24th (Figure 8d,f) and over the Gulf of Mexico in the centre of the simulation domain at 0600 UTC 24 August 2017 (Figure 8g,i). This difference suggests that ABEI effectively inflates the spread in these observed cloudy regions with enhanced convective activity, while CNTL struggles to produce convection in the corresponding regions. Other parts of the model domain outside of the convective regions, such as the west side of the domain at 0000 UTC 24 August 2017, are quite similar between CNTL and ABEI, as is expected by the formulation of ABEI that only inflates where the background prior estimated from the ensemble mean simulates (incorrectly) clear-sky conditions.

Meanwhile, a large ensemble variance with negative C_A scenes are widely spread out in shACI for the first 12 h that contributes to produce convection all across the domain (Figure 8b,e). Although shACI appears to capture the observed convection with reasonable ensemble spreads and small C_A values after 18 h of assimilation at 0600 UTC 24 August 2017 (Figure 8h), the model state space exhibits its deficiency. Figure 9 compares the similar C_A fields as in Figure 8 but for ensemble spread of the sea-level pressure (SLP). The shACI unphysically grows its ensemble SLP standard deviation around the convective centre. Its maximum value reaches 7 hPa, which is much larger than the corresponding values in ABEI and CNTL. Meanwhile, CNTL severely shrinks the ensemble spread, whose standard deviation becomes smaller than 1 hPa across most of the domain. This small ensemble spread severely limits the ability of EnKF to develop new convection. ABEI is able to maintain larger ensemble spread across the domain while avoiding unnecessarily large spread at the convective region around the centre of the domain.

To further examine the impacts of ABEI, Figure 10 compares the performances of each inflation strategy after 18 h of EnKF assimilation valid at 0600 UTC 24 August 2017, when the organized strong convection was actively developing around 92°W, 23°N. The EnKF prior of CNTL contains the developing convection in the centre of the domain (Figure 10a), but it is clearly smaller than the observed regions of clouds, resulting in a ring-shaped large positive prior error (Figure 10b). Because of the difficulty in developing convection in these regions where clear sky is spuriously forecasted outside of the primary convection, most of these positive errors remain in the EnKF posterior (Figure 10c) with a limited analysis increment (Figure 10d). CNTL is also characterized by a small coverage of negative prior error, likely because of the accumulative impacts of the asymmetric performance of CNTL's filter that corrects mostly the negative errors. The shACI appears to be able to develop organized convection with size comparable to the observation. The positive and negative errors in the prior in the observation space are well handled with the EnKF by shACI's large spread that

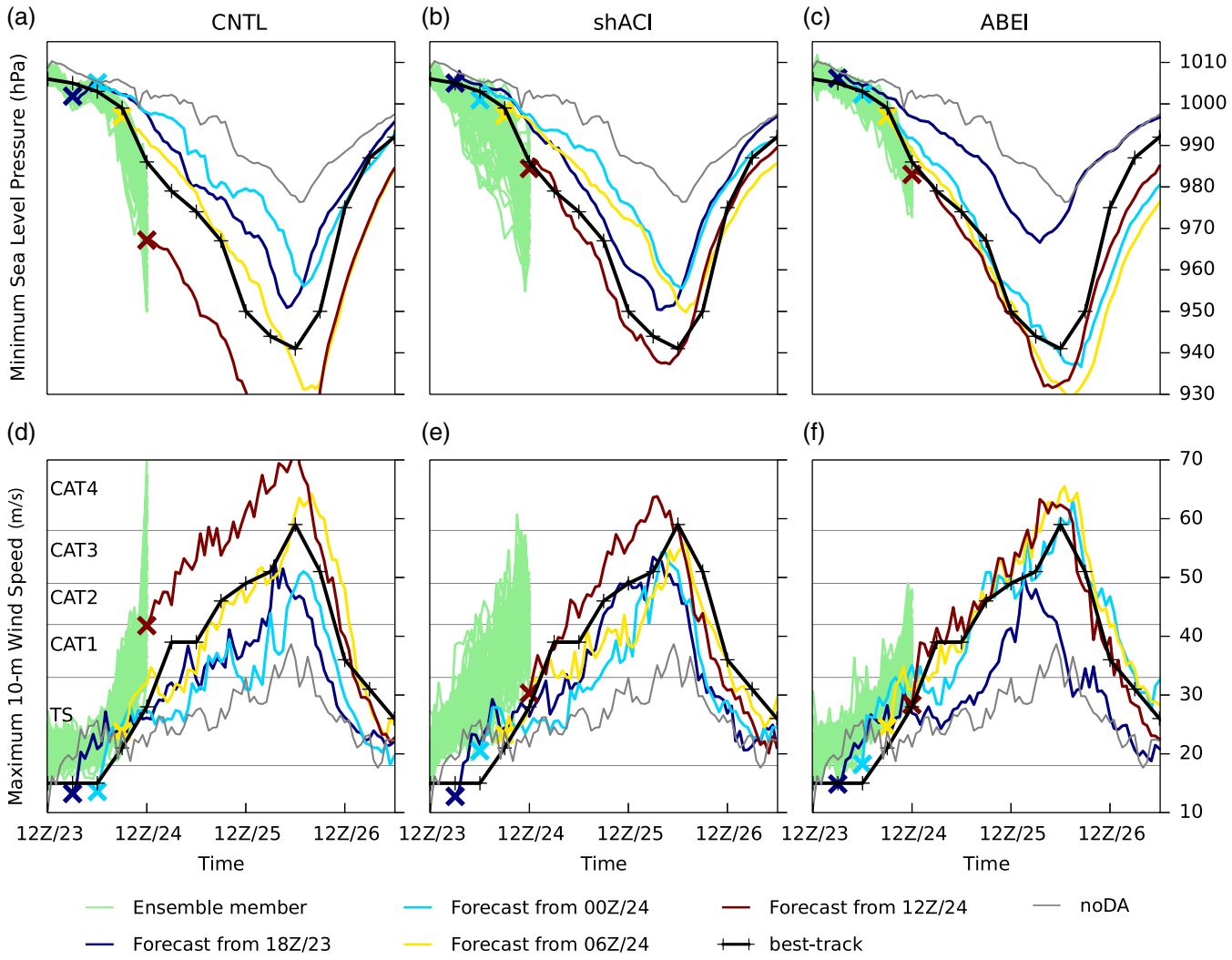

FIGURE 13 Time evolution of tropical cyclone intensity in terms of (a–c) minimum sea-level pressure and (d–f) maximum 10 m wind speed for best-track dataset and different Harvey-OSE analysis and forecast (colour-coded). Results for the (a,b) CNTL, (b,e) shACI and (c,f) ABEI experiment [Colour figure can be viewed at wileyonlinelibrary.com].

overwhelms almost the entire domain (Figure 8e–h). Similarly, although ABEI leaves some positive posterior errors around the southwest edge of convection (and the analysis errors are not as small as shACI), ABEI is also able to better correct most of the prior errors than CNTL.

Similar to Figure 5, the distribution of C_A is compared in Figure 11. Consistent with the Karl-OSSE, applying ABEI greatly suppresses the occurrence of positive C_A scenes, while the negative C_A scenes do not differ as much as positive C_A between CNTL and ABEI. Different from Karl-OSSE, the occurrence of low negative C_A scenes with ABEI becomes more frequent in Harvey-OSE, potentially due to large model error only existing in the real-data assimilation experiment. Because of the chaotic nature of moist convection, the developed convection will not be always able to "hit" the observed convection, but be rather dislocated from observation, which may happen more frequently with an imperfect model, resulting in an increasingly negative C_A scene. Meanwhile, ABEI clearly decreases the occurrence of positive C_A scenes. The shACI behaves similarly to ABEI in positive C_A by decreasing the occurrence of scenes where clear sky is inaccurately estimated in the observed cloudy regions. There is clear difference between shACI and ABEI in negative C_A scenes. The shACI increases the occurrence of negative C_A, likely because shACI uniformly inflates the domain with the exaggerated multiplicative factor estimated in the observation space. This spreads out convection all across the domain, which in turn increases the occurrence of scenes where cloudy sky is inaccurately estimated in observed clear-sky regions. This further highlights the advantage of ABEI to only inflate the empirically under-dispersive situations.

Figure 12 compares the temporal evolutions of RMSE, ensemble spread and consistency ratio in the radiance observation space. The usage of background error inflation in both ABEI and shACI results in smaller RMSEs than CNTL in the late stage of the cycling experiments, in particular after 18 h of assimilation (after 0600 UTC 24th; Figure 12a,b). In CNTL, the improvement at each assimilation cycle gradually decreases, which likely reflects the situation that the prior error is gradually dominated by positive errors that are

difficult to correct. The shACI shows the largest prior and smallest posterior errors for most cycles. Due likely to over-inflation in the entire domain, the prior of the shACI is overwhelmed by clouds that cause a large prior error, while these observed clear-sky regions which are inaccurately estimated as cloudy-sky by the model ensemble prior can be corrected. This feature might result in small errors for EnKF posteriors. CR_y of ABEI is overall closer to one than CNTL, which is consistent with Karl-OSSE (Figure 12c,d). The CR_y values of shACI are the closest to an optimum value of 1.0 for the assimilated channel 8, which is expected because its inflation factor is estimated from the observation space, while it does not significantly differ from ABEI for the independent verification channel 10.

Given that the analyses in the observation space are not always informative enough to evaluate the filter performance, we compare the temporal evolution of the EnKF analysis and forecast of tropical cyclone intensity in Figure 13. The filter-divergence is clearly seen in CNTL due to the lack of sufficient ensemble spreads (Figure 8, left panels). After 18 h of assimilation, the ensemble members of CNTL EnKF start to deviate far from the best-track intensity. The EnKF ensemble mean of CNTL (brown "x" marks in Figure 13c,d) is remarkably more intense than best-track data at 1200 UTC 24 August 2017 by approximately 20 hPa or 15 m/s. The ensemble estimates are also biased high to the more intense side. The shACI is able to avoid the filter divergence and to analyse the EnKF mean field to have comparable intensity to the best-track. The forecast from shACI at 1200 UTC 24 August 2017 (after 24 h of assimilation) well captures the rapid intensification of *Harvey*.

However, ensemble spread keeps increasing in shACI, with the strongest member reaching even category 4 intensity when the EnKF mean and the best-track are still at the tropical storm (TS) category. This again highlights the difficulty in estimating the inflation factor in the observation space, due to the inconsistency between the CR in the observation and the CR in model state space with a nonlinear observation operator. The radiance observation operator exaggerates CR_y compared to the actual CR_x values in the model state space, which in turn unnecessarily inflates the ensemble spread. The application of ABEI is able to provide more reasonable multiplicative inflation factors to constrain the ensemble members and mean around the best-track intensity. Furthermore, all forecasts after 12 h of assimilation almost well capture the rapid intensification, the peak intensity and the rapid decay of *Harvey*, which suggests a better analysis of the tropical cyclone convective structures with ABEI. The initial imbalance and adjustment with ABEI are overall smaller than both shACI and CNTL, which indicates that the improved initial conditions and consistency ratio contributed to reducing the imbalance induced by EnKF update (figures not shown). These results further highlight the advantage of ABEI through better analysing clouds while avoiding localized filter divergence.

5 | CONCLUDING REMARKS

An empirical cloud-scene-dependent ABEI method is proposed for assimilating all-sky satellite brightness temperatures with an ensemble Kalman filter. This study assesses the potentials of using the output of OSSEs to empirically derive the spatially and flow-dependently varying multiplicative covariance inflation factors for various cloud scenes. Filter performance is found to vary among different cloud scenes. Incorrectly modelled clouds are relatively easy to remove because they are shown to be associated with a sufficiently large spread. Meanwhile, an incorrectly modelled clear-sky condition is shown to suffer from insufficient spread to develop clouds. The newly proposed cloud-scene-dependent covariance inflation method only inflates where the background prior estimated from the ensemble mean incorrectly simulates clear-sky conditions in observed cloudy regions, which are shown to be climatologically under-dispersive. We propose the method to empirically calculate the inflation factor by using the cloud scene as a predictor. The empirical method is employed to estimate the consistency ratio (CR) in the model space which alleviates the difficulty in a largely exaggerated CR in the observation space due to strong nonlinearity in the observation operator and the indirect nature of satellite measurements. The impact of this new ABEI method is assessed by assimilating synthetic all-sky radiances in OSSEs for Hurricane *Karl of 2010*, and real-data observations of all-sky BTs from GOES-R ABI in OSEs for Hurricane *Harvey of 2017*, in comparison to the method to adaptively estimate the spatially homogeneous inflation factor (shACI). The shACI method is able to maintain good RMSE and CR values in the observation space, but the ensemble spreads in the model state space are extremely over-inflated. With ABEI, the EnKF analysis of tropical cyclones, as well as the intensity forecast initiated from the EnKF analysis, are shown to be greatly improved. The ABEI method effectively avoids potential local filter divergence without introducing unnecessarily large spread, which contributes to stabilizing the filter performance through long cycling assimilation experiments.

While the ABEI empirically derives the spatial distributions of inflation factors, other methods utilize the spread reduction to obtain the spatial variability, such as those of Anderson (2009), Whitaker and Hamill (2012), Ying and Zhang (2015) and Gharamti (2018). For example, the adaptive RTPP method by Ying and Zhang (2015) directly detects the spread reduction, and the adaptive covariance inflation method by Anderson (2009) assumes the inflation factors and state variables have the same spatial correlation structures, which can also compensate for the spread reduction. Thus, our new inflation method may be regarded as computing the spatially varying "observed" inflation factors, except for accounting for different sources of uncertainty. In this study, the mean of squared difference between the simplified linear inflation model of ABEI and actual CR_x values

are approximately 0.01, which can potentially be used as the uncertainty of the estimated inflation factors by ABEI. Although we directly apply these "observed" inflation factors to focus on the potentials of the new method in this study, the estimated inflation factors can potentially be further combined with other adaptive algorithms in the ensemble data assimilation and in assimilating highly nonlinear observations such as the all-sky microwave radiances. These potentials will be further investigated in future studies, together with more systematic evaluations of the proposed empirical inflation method for different satellite platforms with a large number of cases, in comparison and potentially combining with other existing spatially varying adaptive inflation methods.

ACKNOWLEDGEMENTS

This research is partially supported by ONR Grants N000141512298 and N000141812517, and NASA Grants NNX16AD84G and NNX15AQ51G. MM was also supported by Japan's Funai Overseas Scholarship of the Funai Foundation for Information Technology. We benefited from discussions with Yunji Zhang and many others. Computing was provided by the Texas Advanced Computing Center (TACC). All data presented are stored and can be accessed through the TACC data archive. The authors have no conflict of interest with the study.

ORCID

Fuqing Zhang https://orcid.org/0000-0003-4860-9985

REFERENCES

Anderson, J.L. (2007) An adaptive covariance inflation error correction algorithm for ensemble filters. *Tellus, Series A: Dynamic Meteorology and Oceanography*, 59(2), 210–224. http://doi.org/10.1111/j.1600-0870.2006.00216.x.

Anderson, J.L. (2009) Spatially and temporally varying adaptive covariance inflation for ensemble filters. *Tellus A*, 61(1), 72–83. http://doi.org/10.1111/j.1600-0870.2008.00361.x.

Auligné, T., Lorenc, A., Michel, Y., Montmerle, T., Jones, A., Hu, M. and Dudhia, J. (2011) Toward a new cloud analysis and prediction system. *Bulletin of the American Meteorological Society*, 92(2), 207–210. http://doi.org/10.1175/2010BAMS2978.1.

Bauer, P., Geer, A.J., Lopez, P. and Salmond, D. (2010) Direct 4D-Var assimilation of all-sky radiances. Part I: Implementation. *Quarterly Journal of the Royal Meteorological Society*, 136(652), 1868–1885. http://doi.org/10.1002/qj.659.

Bauer, P., Lopez, P., Benedetti, A., Salmond, D. and Moreau, E. (2006) Implementation of 1D+4D-Var assimilation of precipitation-affected microwave radiances at ECMWF. I: 1D-Var. *Quarterly Journal of the Royal Meteorological Society*, 132(620), 2277–2306. http://doi.org/10.1256/qj.05.189.

Bauer, P., Ohring, G., Kummerow, C. and Auligne, T. (2011) Assimilating satellite observations of clouds and precipitation into NWP models. *Bulletin of the American Meteorological Society*, 92(6), 25–28. http://doi.org/10.1175/2011BAMS3182.1.

Dee, D.P. (1995) Online estimation of error covariance parameters for atmospheric data assimilation. *Monthly Weather Review*, 123(4), 1128–1145. http://doi.org/10.1175/1520-0493(1995)123<1128:OLEOEC>2.0.CO;2.

Desroziers, G., Berre, L., Chapnik, B. and Poli, P. (2005) Diagnosis of observation, background and analysis-error statistics in observation space. *Quarterly Journal of the Royal Meteorological Society*, 131(613), 3385–3396. http://doi.org/10.1256/qj.05.108.

Errico, R.-M., Bauer, P. and Mahfouf, J.-F. (2007) Issues regarding assimilation of cloud and precipitation data. *Journal of the Atmospheric Sciences*, 64(11), 3785–3798. http://doi.org/doi:10.1175/2006JAS2044.1.

Geer, A.J. and Bauer, P. (2011) Observation errors in all-sky data assimilation. *Quarterly Journal of the Royal Meteorological Society*, 137(661), 2024–2037. http://doi.org/10.1002/qj.830.

Gharamti, M.E. (2018) Enhanced adaptive inflation algorithm for ensemble filters. *Monthly Weather Review*, 146, 623–640. http://doi.org/10.1175/MWR-D-17-0187.1.

Han, Y., van Delst, P., Liu, Q., Weng, F., Yan, B., Treadon, R. and Derber, J. (2006) JCSDA Community Radiative Transfer Model (CRTM) - Version 1, *NOAA Technical Report NESDIS*, 122, 40 pp. [Available online at https://repository.library.noaa.gov/view/noaa/1157.]

Han, Y., Weng, F., Liu, Q. and van Delst, P. (2007) A fast radiative transfer model for SSMIS upper atmosphere sounding channels. *Journal of Geophysical Research*, 112(D11), D11121. http://doi.org/10.1029/2006JD008208.

Harnisch, F., Weissmann, M. and Periáñez, Á. (2016) Error model for the assimilation of cloud-affected infrared satellite observations in an ensemble data assimilation system. *Quarterly Journal of the Royal Meteorological Society*, 142(697), 1797–1808. http://doi.org/10.1002/qj.2776.

Heidinger, A.K., O'Dell, C., Bennartz, R. and Greenwald, T. (2006) The successive-order-of-interaction radiative transfer model. Part I : Model development. *Journal of Applied Meteorology and Climatology*, 45(10), 1388–1445.

Honda, T., Miyoshi, T., Lien, G.-Y., Nishizawa, S., Yoshida, R., Adachi, S.A., Terasaki, K., Okamoto, K., Tomita, H. and Bessho, K. (2018) Assimilating all-sky Himawari-8 satellite infrared radiances: a case of typhoon *Soudelor* (2015). *Monthly Weather Review*, 146(1), 213–229. http://doi.org/10.1175/MWR-D-16-0357.1.

Hong, S. and Lim, J. (2006) The WRF single-moment 6-class microphysics scheme (WSM6). *Journal of the Korean Meteorological Society*, 42(2), 129–151.

Hong, S.-Y., Noh, Y. and Dudhia, J. (2006) A new vertical diffusion package with an explicit treatment of entrainment processes. *Monthly Weather Review*, 134(9), 2318–2341. http://doi.org/10.1175/MWR3199.1.

Iacono, M.J., Delamere, J.S., Mlawer, E.J., Shephard, M.W., Clough, S.A. and Collins, W.D. (2008) Radiative forcing by long-lived greenhouse gases: calculations with the AER radiative transfer models. *Journal of Geophysical Research: Atmospheres*, 113(13), 2–9. http://doi.org/10.1029/2008JD009944.

Jones, T.A., Otkin, J.A., Stensrud, D.J. and Knopfmeier, K. (2013) Assimilation of satellite infrared radiances and Doppler radar observations during a cool season observing system simulation experiment. *Monthly Weather Review*, 141(10), 3273–3299. http://doi.org/10.1175/MWR-D-12-00267.1.

Jones, T.A., Otkin, J.A., Stensrud, D.J. and Knopfmeier, K. (2014) Forecast evaluation of an observing system simulation experiment assimilating both radar and satellite data. *Monthly Weather Review*, 142(1), 107–124. http://doi.org/10.1175/MWR-D-13-00151.1.

Kotsuki, S., Ota, Y. and Miyoshi, T. (2017) Adaptive covariance relaxation methods for ensemble data assimilation: experiments in the real atmosphere. *Quarterly Journal of the Royal Meteorological Society*, 143(705), 2001–2015. http://doi.org/10.1002/qj.3060.

Li, H., Kalnay, E. and Miyoshi, T. (2009) Simultaneous estimation of covariance inflation and observation errors within an ensemble Kalman filter. *Quarterly Journal of the Royal Meteorological Society*, 135(639), 523–533.

Minamide, M. and Zhang, F. (2017) Adaptive observation error inflation for assimilating all-sky satellite radiance. *Monthly Weather Review*, 145, 1063–1081. http://doi.org/10.1175/MWR-D-16-0257.1.

Minamide, M. and Zhang, F. (2018) Assimilation of all-sky infrared radiances from Himawari-8 and impacts of moisture and hydrometeor initialization on convection-permitting tropical cyclone prediction. *Monthly Weather Review*, 146(10), 3241–3258. http://doi.org/10.1175/MWR-D-17-0367.1.

Mitchell, H.L. and Houtekamer, P.L. (2000) An adaptive ensemble Kalman filter. *Monthly Weather Review*, 128(2), 416–433. http://doi.org/10.1175/1520-0493(2000)128<0416:AAEKF>2.0.CO;2.

Okamoto, K., McNally, A.P. and Bell, W. (2014) Progress towards the assimilation of all-sky infrared radiances: an evaluation of cloud effects. *Quarterly Journal of the Royal Meteorological Society*, 140(682), 1603–1614. http://doi.org/10.1002/qj.2242.

Otkin, J.A. (2010) Clear and cloudy sky infrared brightness temperature assimilation using an ensemble Kalman filter. *Journal of Geophysical Research: Atmospheres*, 115, 1–14. http://doi.org/10.1029/2009JD013759.

Otkin, J.A. (2012) Assimilation of water vapor sensitive infrared brightness temperature observations during a high impact weather event. *Journal of Geophysical Research: Atmospheres*, 117, 1–16. http://doi.org/10.1029/2012JD017568.

Parrish, D.F. and Derber, J.C. (1992) The National Meteorological Center's spectral statistical-interpolation analysis system. *Monthly Weather Review*, 120(8), 1747–1763. http://doi.org/10.1175/1520-0493(1992)120<1747:TNMCSS>2.0.CO;2.

Skamarock, W.C., Klemp, J.B., Dudhi, J., Gill, D.O., Barker, D.M., Duda, M.G., Huang, X.Y., Wang, W.a. and Powers, J.G. (June 2008) *A description of the advanced research WRF Version 3. NCAR Technical Note*, NCAR/TN-4751STR, 113. http://doi.org/10.5065/D6DZ069T.

Tiedtke, M. (1989) A comprehensive mass flux scheme for cumulus parameterization in large-scale models. *Monthly Weather Review, 117, 1779–1800.* http://doi.org/10.1175/1520-0493(1989)117<1779:ACMFSF>2.0.CO;2.

Vukicevic, T., Greenwald, T., Zupanski, M., Zupanski, D., Vonder Haar, T. and Jones, A.S. (2004) Mesoscale cloud state estimation from visible and infrared satellite radiances. *Monthly Weather Review*, 132(12), 3066–3077. http://doi.org/10.1175/MWR2837.1.

Wang, P., Li, J., Goldberg, M.D., Schmit, T.J., Lim, A.H.N., Li, Z.L. and Ackerman, S.A. (2015) Assimilation of thermodynamic information from advanced infrared sounders under partially cloudy skies for regional NWP. *Journal of Geophysical Research: Atmospheres*, 120(11), 5469–5484. http://doi.org/10.1002/2014JD022976.

Weng, F. (2007) Advances in radiative transfer modeling in support of satellite data assimilation. *Journal of the Atmospheric Sciences*, 64(11), 3799–3807. http://doi.org/10.1175/2007JAS2112.1.

Weng, Y. and Zhang, F. (2012) Assimilating airborne Doppler radar observations with an ensemble Kalman filter for convection-permitting hurricane initialization and prediction: *Katrina* (2005). *Monthly Weather Review*, 140(3), 841–859. http://doi.org/10.1175/2011MWR3602.1.

Weng, Y. and Zhang, F. (2016) Advances in convection-permitting tropical cyclone analysis and prediction through EnKF assimilation of reconnaissance aircraft observations. *Journal of the Meteorological Society of Japan*, 94(4), 345–358. http://doi.org/10.2151/jmsj.2016-018.

Whitaker, J.S. and Hamill, T.M. (2012) Evaluating methods to account for system errors in ensemble data assimilation. *Monthly Weather Review*, 140(9), 3078–3089. http://doi.org/10.1175/MWR-D-11-00276.1.

Ying, Y. and Zhang, F. (2015) An adaptive covariance relaxation method for ensemble data assimilation. *Quarterly Journal of the Royal Meteorological Society*, 141(692), 2898–2906. http://doi.org/10.1002/qj.2576.

Zhang, F., Minamide, M. and Clothiaux, E.E. (2016) Potential impacts of assimilating all-sky infrared satellite radiances from GOES-R on convection-permitting analysis and prediction of tropical cyclones. *Geophysical Research Letters*, 43, 2954–2963. http://doi.org/10.1002/2016GL068468.

Zhang, F., Snyder, C. and Sun, J. (2004) Impacts of initial estimate and observation availability on convective-scale data assimilation with an ensemble Kalman filter. *Monthly Weather Review*, 132(5), 1238–1253. http://doi.org/10.1175/1520-0493(2004)132<1238:IOIEAO>2.0.CO;2.

Zhang, F., Weng, Y., Gamache, J.F. and Marks, F.D. (2011) Performance of convection-permitting hurricane initialization and prediction during 2008–2010 with ensemble data assimilation of inner-core airborne Doppler radar observations. *Geophysical Research Letters*, 38(15), L15810. http://doi.org/10.1029/2011GL048469.

Zhang, F., Weng, Y., Sippel, J.A., Meng, Z. and Bishop, C.H. (2009) Cloud-resolving hurricane initialization and prediction through assimilation of Doppler radar observations with an ensemble Kalman filter. *Monthly Weather Review*, 137(7), 2105–2125. http://doi.org/10.1175/2009MWR2645.1.

Zou, X., Qin, Z. and Zheng, Y. (2015) Improved tropical storm forecasts with GOES-13/15 imager radiance assimilation and asymmetric vortex initialization in HWRF. *Monthly Weather Review*, 143(7), 2485–2505. http://doi.org/10.1175/MWR-D-14-00223.1.

Zou, X., Weng, F., Zhang, B., Lin, L., Qin, Z. and Tallapragada, V. (2013) Impacts of assimilation of ATMS data in HWRF on track and intensity forecasts of 2012 four landfall hurricanes. *Journal of Geophysical Research: Atmospheres*, 118(20), 11558–11576. http://doi.org/10.1002/2013JD020405.

How to cite this article: Minamide M, Zhang F. An adaptive background error inflation method for assimilating all-sky radiances. *Q J R Meteorol Soc* 2019;1–19. https://doi.org/10.1002/qj.3466